DIRECT INK WRITING OF FORSTERITE POROUS STRUCTURE

TAN WEI SHIN

UNIVERSITI TUNKU ABDUL RAHMAN

DIRECT INK WRITING OF FORSTERITE POROUS STRUCTURE

TAN WEI SHIN

**A project report submitted in partial fulfilment of the
requirements for the award of Bachelor of Mechanical Engineering
with Honours**

**Lee Kong Chian Faculty of Engineering and Science
Universiti Tunku Abdul Rahman**

May 2024

DECLARATION

I hereby declare that this project report is based on my original work except for citations and quotations which have been duly acknowledged. I also declare that it has not been previously and concurrently submitted for any other degree or award at UTAR or other institutions.

Signature : _____

Name   : Tan Wei Shin

ID No.   : 2002754

Date   : 20/4/2024

APPROVAL FOR SUBMISSION

I certify that this project report entitled **"DIRECT INK WRITING OF FORSTERITE POROUS STRUCTURE"** was prepared by **TAN WEI SHIN** has met the required standard for submission in partial fulfilment of the requirements for the award of Bachelor of Mechanical Engineering with Honours at Universiti Tunku Abdul Rahman.

Approved by,

Signature   :   _____

Supervisor   :   Dr Khaw Chwin Chieh

Date   :   22/4/2024

Signature   :   _____

Co-Supervisor :   Dr Yeo Wei Hong

Date   :   22/4/2024

The copyright of this report belongs to the author under the terms of the copyright Act 1987 as qualified by Intellectual Property Policy of Universiti Tunku Abdul Rahman. Due acknowledgement shall always be made of the use of any material contained in, or derived from, this report.

ACKNOWLEDGEMENTS

I would like to express my sincere gratitude to everyone who has played a part in the successful completion of this project.

First and foremost, my heartfelt thanks go to Dr. Yeo Wei Hong and Dr. Khaw Chwin Chieh for their unwavering support and expert guidance throughout the development of this work. Their profound knowledge and insightful suggestions have been instrumental in shaping this project from its inception to its completion. I am deeply grateful for their patience and commitment, which provided me with a strong foundation to navigate the challenges of this work.

I would also like to extend my appreciation to senior Wong Zong Qi and Ang Xiang for their continuous help and advice. Their generous support, constructive feedback, and willingness to share their experiences have made a significant impact on my ability to conduct and complete this project. Their mentorship and encouragement have been invaluable, and I am truly fortunate to have had them as part of my support network.

Thank you all for your contributions. Your involvement has not only enriched this project but has also been a source of inspiration and motivation for me

ABSTRACT

Additive manufacturing (AM), which also known as 3D printing. Its popularity has soared due to its design flexibility, rapid prototyping, and reduced material waste. For example, biomedical engineering in recent years is aiming to achieve bone regeneration by 3D printing due to its ability to control precisely the porous structure for bioceramic. Magnesium-based bioceramics, such as forsterite emerged as a new class of promising biodegradable materials, due to its good degradation and biocompatibility. Nowadays, 3D printing material with forsterite primarily uses water-based solvents. Beside water-based, organic solvents provide some additional advantages such as better mechanical properties. Therefore, the main objective of this project is to obtain the optimum formulation of forsterite with organic solvents. Additionally, the rheology and physical properties are also studied. The study began with synthesis of forsterite powder. Then, different formulations from 35 vol% to 45 vol% of forsterite loading, 300 g/L to 400 g/L of binder concentration, 15 vol% of plasticiser and 10 vol% of dispersants are tested. The combination of 43 vol% and 40 vol% with binder concentration of 400 g/L showed the best result in printability test. 43 vol% forsterite loading ink shows greater storage modulus and loss modulus than 40 vol%, which had 28.05 Pa of yield shear stress and 4183.60 Pa of flow shear stress. Sintered part of 43 vol% also have better performance than 40 vol% in terms of physical properties such as dimension shrinkage at 18.83 %, weight reduce at 17.04 % and density at 2.70 g/cm^3. 43 vol% ink also has greater hardness than 40 vol% ink. In conclusion, the optimum formulation of forsterite DIW ink is 43 vol% forsterite loading, 400 g/L binder concentration, 32 vol% binder solution, 15 vol% plasticiser and 10 vol% dispersant. Thus, this study provides reference for the future study of forsterite organogel ink.

TABLE OF CONTENTS

LIST OF TABLES

LIST OF FIGURES

LIST OF SYMBOLS / ABBREVIATIONS

h	layer-to-layer height, mm
s	span length
M	mass flow rate, kg/s
P	porosity, %
P_{micro}	micro porosity, %
P_{macro}	macro porosity, %
P_a	apparent porosity, %
P_t	close porosity, %
Q	volumetric flow rate, mm^3/s
S	printing speed, mm/s
R	radius of nozzle, mm
ID	inner diameter of nozzle, mm
$\dot{\gamma}$	shear rate, s^{-1}
ρ	density, kg/m^3
G'	storage modulus
G"	loss modulus

DIW	Direct Ink Writing
HPMC	Hydroxypropylmethylcellulose
CDB	Cellulose Derivative Binder
XRD	X-Ray Diffraction
SEM	Scanning Electron Microscope
3ITT	Three Interval Thixotropy Test

LIST OF APPENDICES

CHAPTER 1

INTRODUCTION

1.1   General Introduction

Additive Manufacturing (AM) is a manufacturing technique that generates three-dimensional objects by progressively depositing materials. Different with conventional and traditional manufacturing, which include the process procedures such as casting, forging, welding, and machining, AM allows parts to be made directly based on computer data and is particularly suitable for complex or customized structures. When combined with computer-aided design (CAD), AM has gained prominence in the realms of rapid prototyping and customized design solutions. This prominence arises from the remarkable design flexibility offered by additive manufacturing, enabling the creation of highly optimized components that would be cost-prohibitive or even unfeasible using alternative manufacturing methods (Jinge and Peng, 2022). In such cases, the term "rapid manufacturing" is often used, although it is somewhat misleading, as the process itself is not inherently swift. While it may not always be the fastest method of production, the advantages it offers in terms of design, time to market, iterative development, and cost savings make it an invaluable tool for businesses seeking to innovate and stay competitive in today's dynamic market.

Forsterite is used as the material of direct ink writing in this paper. Forsterite with the chemical formula Mg_2SiO_4 which exhibits an impressive melting point, reaching as high as 1890°C (Ratnawulan and Ahmand, 2020). Therefore, it qualifies as one of the fundamental super refractories required for numerous applications. For example, one of the applications is its use as a construction material for devices controlling the flow of molten metal in the steel industry. Other than that, it also serves as lining and coating material for steel ladles, which are utilized to gather molten metal during the production of alloys and smelting processes. Basic materials such as magnesite and dolomite have excellent corrosion resistance and high temperature resistance compared to alumina silicate refractories, so they are favoured by the steel industry. These basic materials, based primarily on magnesium oxide (MgO) compounds such

as forsterite, have the potential to provide refractory linings that perform better than commonly used materials. Additionally, forsterite has different physical and chemical properties from other minerals, which making it a promising alternative.

Other than that, forsterite has attracted a lot of interest from scientists as a bioceramic in recent years. Forsterite contains silicon (Si) and magnesium (Mg), both of which are known to have a significant role in the development and mineralization of bones in the human body. It has been proven that silicate-containing substances, including larnite, calcium silicate, and tricalcium silicate, have exceptional bioactivity in both lab settings and living creatures. These silicate-based material were found as a suitable candidate for hard tissue and soft tissue regeneration. Forsterite stands out among all the member of silicate-based bioceramics, due to its impressive mechanical strength and gradual degradation in bodily fluids. These attributes make it a promising option for repairing hard tissues within the body. For example, forsterite has noticeably higher resistance to fracture than its close relative, cadmium ($MgSiO_3$), when it is thought of as viable biomaterial for prosthetic implants.

Due to the biocampability of forsterite, 3D printability of porous structure is aimed to study. When a substance is biologically integrated, it signifies that the body reacts favourably to its presence and that it becomes a part of the biological system. The porous structure of important due to tissue ingrowth. During the tissue repair and regeneration, body cells should Gradually penetrate and grows into the material. This process is facilitated by the presence of porous structures or surface features that promote cell adhesion and migration. For tissues to survive, a sufficient blood flow is essential. The development of new blood vessels inside and surrounding the implanted material is crucial for biointegration. This makes sure that cells and surrounding tissue around the implant receive nutrition and oxygen (Shakib, et at., 2022). Other than biological integration, porous structure also important in term of industrial application to decrease density and increase elastic modulus. Porous forsterite can act as an excellent thermal insulator. Its low thermal conductivity makes it effective at preventing the transfer of heat, making it valuable in high-temperature environments where insulation is crucial.

1.2   Importance of the Study

This project is to find out the optimum formulation for 3D print forsterite porous structure via direct ink method. From a materials science perspective, the purity of forsterite plays a vital role in ensuring the final quality of printed materials. Other than that, the rheological behaviour of the material also plays a crucial role in ensuring smooth extrusion through the 3D printer's extruder head. Therefore, formulation of ceramic ink is important to ensure the printability. For example, the materials selection for organic solvent, binder and other such as dispersant, and the ratio for them. The method to porosity of structure after sintering is also one of the important points to study. By conducting series of testing and analysing, printed material of forsterite can optimize its physical property and mechanical property such as density and hardness. This will provide reference for the future study of the DIW of forsterite with organic solvent to produce a forsterite orgagonel ink in terms of compatibility, printability, physical and mechanical properties. Other than that, forsterite also having a high potential to become the mainstream material for bioceramic. This provide the better physical and mechanical properties for the implantation of bone and tissue in bioengineering field.

1.3   Problem Statement

There was a study conducted by Monica, et al (2021) regarding the preparation of crystalline bioceramics through the calcination of either moulded or 3D printed magnesium silicate hydrate (M–S–H) cements. This research focused on the hydration of MgO/SiO_2, which produces cement pastes composed of both M–S–H binder and brucite in varying amounts depending on the Mg/Si ratio and the source of silica. Since there is research about the 3D printed bioceramic made from Mg/Si material with water solvent. Therefore, this project aims to produce forsterite as one of the Mg/Si based bioceramic DIW ink with other type of solvent. Although the importance of porosity in bioceramic is mentioned in the study of Monica, et al (2021). However, there is no detail discussion about the porosity control in the research. Thus, this research also aims to produce the porosity of DIW ink in terms of macro and micro.

Therefore, this project was aimed to optimize the formulation of forsterite ceramic ink in term of printability and rheology behaviour. The study of porosity was also conducted in terms of ink formulation and its physical and mechanical properties.

1.4   Aim and Objectives

The primary goal of this project was to is to formulate ceramic ink for 3D print forsterite porous structure via direct ink method. The following were the specific objectives of this study to accomplish:

1) Synthesise forsterite powder using mechanical activation method.
2) Formulate forsterite-cellulose composition suitable for direct ink writing of porous structure.
3) Evaluate the rheology behaviour and printability of the formulated ceramic ink.
4) Evaluate the physical properties and microstructure morphology after sintering process.

1.5   Scope and Limitation of the Study

In this research project, many laboratory instruments were employed, including high shear mixer, oven, furnace to prepare forsterite. The microstructure of the samples will be examined using X-ray diffraction (XRD). Several tests are conducted to formulate the forsterite ceramic slurry. For example, sedimentation test for dispersant in different composition of solvent and solubility test for cellulose derivative as binder. Rheological investigations were carried out using analytical tools such as a rheometer, in conjunction with relevant analytical software. Lastly, a 3D printer was used to test the printability of slurry and define the optimal printing parameter. Then, performed density test by investigate the water immersion of it.

For the limitation, the solid loading during the formulate forsterite-cellulose compositions were limited to 45%, 43%, 40% and 35% due to the time constraint. A constant temperature of 1500°C is used for the sintering process. Other than that, density test was one of the methods for studying porosity, but it cannot obtain the full complexity of pore structures and distribution.

Complementary techniques, such as micro-CT, could provide a more comprehensive analysis.

1.6   Contribution of the Study

In this project, the ceramic ink for 3D print forsterite porous structure via direct ink method was formulated. This study was explored the compatibility of acetone-based ink (organogel ink) with forsterite. The organogel forsterite ink provide better mechanical and physical properties of printed structure. Therefore, in biomedical engineering, a bone regenerative with improved mechanical property can be achieved. The optimum formulation of forsterite ceramic has been explored. The new study of rheological behaviour of forsterite organogel ink with different solid loading also explored. In terms of additive manufacturing field, it provides a reference for further study of forsterite organogel ink.

1.7   Outline of the Report

The following Chapter 2 was discussed about the literature review on direct ink writing, forsterite, method to synthesis of forsterite, choose of binder and solvent for the ceramic ink, organogel ink, rheology factor and also porosity of ceramic structure. After that, Chapter 3 was further discussed about the methodology on the synthesis of forsterite, ceramic ink preparation and printing process. The methodology of analysis was also be discussed, such as rheology analysis, density test, Vickers hardness test, optical microscopy and SEM. Then, the analysed results of XRD, printability, rheology behaviour, SEM, physical properties such as shrinkage, weight loss, density and porosity as well as mechanical property such as Vickers hardness was discussed in Chapter 4. Lastly, Chapter 5 is the conclusion and recommendations for future work.

CHAPTER 2

LITERATURE REVIEW

2.1 Direct Ink Writing (DIW)

Direct Ink Writing (DIW), also referred to as Direct Write Fabrication, Robocasting, or Robot-Assisted Shape Deposition, is one of a material extrusion process. Cesarani et al. developed it at Sandia National Laboratories in 1997 to produce concentrated materials such as ceramic pastes containing some organic binder (Aamir and Ismail, 2021). It is an additive manufacturing process that emphasizes precise material deposition using high-viscosity inks, pastes, or gels, enabling the creation of intricate 3D structures. Unlike FDM, DIW does not rely on the extrusion of solid filaments or photo-polymerization but depends on syringe cartridge paste deposition with characteristics (Jennifer, 2006). Each complex fluid is made up of a fraction of powdered materials with addictive substances mixed in.

This approach is simple, versatile, and affordable, and it is suitable for a wide range of materials, including ceramic materials (monolithic and composites), polymers, alloys, and food. Despite its potential, DIW still faces challenges such as the slurry preparation. During the extrusion through the nozzle, the viscosity of the produced ink must exhibit shear thinning behaviour. At the same time, the fluid viscosity, yield strength, and stiffness must be sufficient to maintain the rigidity of printed material. (Aamir and Ismail, 2021). Other than that, many DIW-printed structures require post-processing steps, such as drying, sintering, or curing, which can be time-consuming and labour-intensive (Hinton, et al., 2015).

Direct Ink Writing (DIW) in 3D printing has shown to be extremely versatile across a wide range of applications. For example, in the field of bioprinting, enabling precise deposition of living cells and biomaterials. With this ability, it is offering potential in tissue engineering (Hinton, et al., 2015). Furthermore, its flexibility lends itself perfectly to soft robotics, yielding supple actuators, grippers, and wearable devices for safe and adaptable human-machine interactions (Robert F et al., 2011). Moreover, there are also other application of DIW such as aerospace, electronics and construction.

Despite the obstacles, DIW enables the production of complicated forms without the need of a mould or typical processes. Its accuracy, material diversity, and wide range of applications have propelled it to the forefront of additive manufacturing. And, as materials and methods improve, DIW's importance in additive manufacturing is set to grow.

2.2   Analysis of forsterite

Forsterite is a crystalline magnesium silicate with the chemical formula Mg_2SiO_4 that was named after the German chemist Johann Forster. It is found in the magnesia-silica system and belongs to the olivine group with an orthorhombic structure (Tavangarian and Emadi, 2010). Forsterite is a mineral that is frequently utilised in electronics, communication, and refractory applications. Because of its low dielectric loss with regard to extremely high-frequency electromagnetic waves, forsterite ceramics are employed as a dielectric material in high frequency circuits such as submillimetre-wave applications (Upik Nurbaiti, et al., 2018). High-frequency circuits operate at frequencies that are far higher than those seen in conventional electronics. They're employed in high-tech communication systems, radar technology, and a variety of scientific and industrial applications. Maintaining the integrity and efficiency of electromagnetic signals is critical in such circuits. Forsterite was employed as a solid oxide fuel cell because it can retain high stability and has a linear thermal expansion rate that matches other materials used in fuel cells. The height stability refers to forsterite is employed in solid oxide fuel cells due to its ability to maintain structural integrity and chemical stability, even under high-temperature and corrosive operating conditions. And when the fuel cell is exposed to temperature changes during operation, forsterite and the surrounding materials will expand and contract at similar rates. Therefore, it reduces the risk of cracking or structural damage. It has a high melting point up to 1890 ℃, strong refractoriness and low heat conductivity, and an efficient microwave dielectric (Kosanović, et al., 2005).

High performance of forsterite is due to forsterite consists of the Mg^{2+} cation and SiO_4^{4-} anion in a molar ratio of 2:1. Each oxygen atom within the $SiO4^{4-}$ anion is connected to the core silicon atom by a single covalent connection. The covalent link between the oxygen atom and the silicon atom,

the four oxygen atoms must be kept apart to lessen the repulsive force between them. This is due to the partial negative charge. The arrangement of the atoms produces a tetrahedral structure (Iishi, 1978). Therefore, Forsterite crystallizes in an orthorhombic crystal system, which means it has three axes of unequal length, each intersecting at 90-degree angles. The crystal structure of forsterite consists of corner-sharing SiO_4 tetrahedra and MgO_6 octahedra (Iishi, 1978). With oxygen atoms spanning between silicon and magnesium cations, this arrangement produces a three-dimensional framework.

2.2.1   Material selection for forsterite synthesis

There are a lot of combination for the synthesis of forsterite. Generally, from the structure of forsterite (Mg_2SiO_4), it requires both magnesium source and silica source to from a forsterite structure. For the silica source, the common material found in market are precipitated silica, hydrophilic fume silica, talc and silica gel. And the common material for magnesium source is only limited to magnesium oxide, magnesium carbonate and magnesium nitrate.

Magnesium oxide is used as the magnesium source due to ion contain in magnesium oxide. Forsterite has the chemical formula Mg_2SiO_4, which implies that the crystal structure has a 1:1 ratio of magnesium ions to silicon ions. Magnesium oxide (MgO) delivers magnesium ions in a 1:1 ratio, which is compatible with forsterite's stoichiometry (Simon, et al., 2017). For magnesium carbonate, another step and reaction required to conduct to release magnesium ion (Tavangarian and Emadi, 2009).

$$5MgCO_3 \rightarrow 5MgO + 5CO_2 \qquad (2.1)$$
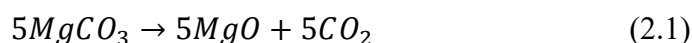
Then, to define the best option for silica source, the particle size is studied. The talc powder particles were lamellar in shape with a mean particle size of about 20 μm (Tavangarian and Emadi, 2009). And like discussed on last paragraph, talc also required additional step and reaction to ensure talc have reacted with MgO to produce enstatite ($MgSiO_3$). Then, the enstatite only able to react with MgO again to produce forsterite (Kosanović, et al., 2005).

$$Mg_3Si_4O_{10}(OH)_2 + MgO \rightarrow 4MgSiO_3 + H_2O \qquad (2.2)$$

$$MgO + MgSiO_3 \rightarrow Mg_2SiO_4 \qquad\qquad (2.3)$$
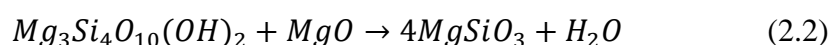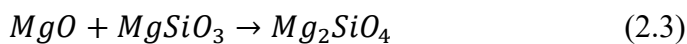
The range of particle size of precipitate silica is up to 0.2 µm, and up to 63 µm for silica gel. The particle size of hydrophilic fume silica is only less than 0.1µm (Runxiao, Tanvier and Daman, 2022). The smaller particle size is choosing due to its higher surface area and may offer enhanced reactivity and potentially more precise control over the synthesis process.

2.3 Method for Synthesis of forsterite

There are many methods to synthesize forsterite which already developed. For example, mechanical activation of ball milling, mechanical activation of high hear mixer and other.

2.3.1 Mechanical activation (Ball Milling)

Over the past few years, there has been a growing interest in ball milling technique, leading to the development of numerous high-quality synthetic methods that encompass the entire spectrum of organic synthesis. (Achim Stolle et al., 2011). Ball milling is a mechanical technique that includes continuously impacting particles with milling balls inside a revolving container to grind and reduce them. Collisions and friction between the balls and the material cause particles to break apart, reducing their size and attaining homogeneity. This adaptable approach was extensively employed in a variety of sectors for activities like as particle size reduction, mixing, and material synthesis, providing precise control over the end product's qualities.

For the synthesis of nanocrystalline materials, solid state reaction, also known as mechanical activation or high energy ball milling, has been frequently employed (Claudio and Brian, 2002). There are no specific procedure or parameter for ball milling. For example, a hardened steel vial of 125 ml with five 20 mm steel balls can be use as milling media. The ball-to-powder weight ratio was roughly 10:1 in all milling runs, and the main disc rotational speed was set at 500 rpm. The maximum milling duration was 60 hours, and annealing was done in the air at 1000 and 1200ºC for 1 hour (Tavangarian and Emadi, 2010). And contamination of fluorine and chlorine ions were discovered but can

be eliminate by increase the duration of forsterite production during the mechanical activation process (Tavangarian and Emadi, 2010).

However, the higher ball milling time does not mean will obtain a smaller crystallite size of particle. From Figure 2.1 Crystallite sizes of forsterite phase as a function the time of mechanical activation and subsequent annealing. It shows that no fixed pattern of change of the crystallite size of particle along time. Therefore, duration of ball milling shows no significant effect to the crystallite size of forsterite (Tavangarian and Emadi, 2009).
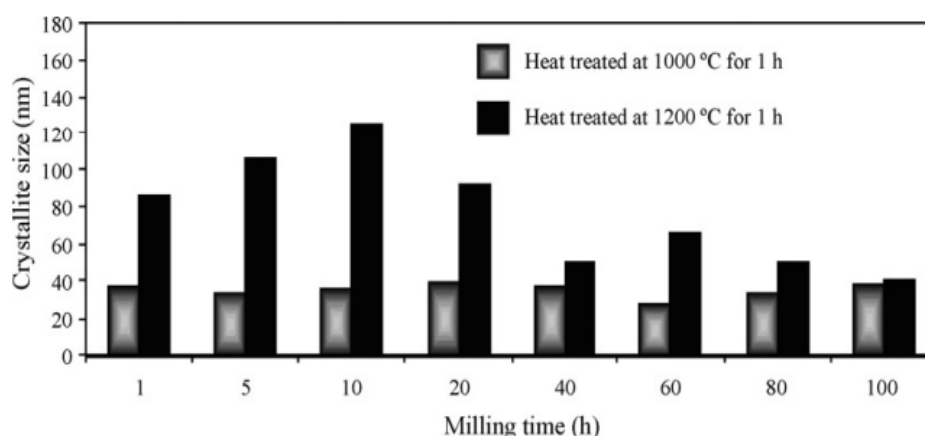
Figure 2.1: Crystallite sizes of forsterite phase as a function the time of mechanical activation and subsequent annealing (Tavangarian and Emadi, 2009).

2.3.2   Mechanical activation (High Shear Mixer)

There are certain drawbacks to ball milling. Even for mixing operations that do not have the express purpose of particle size reduction, it can take up to 8 - 24 hours. These procedures consume a lot of energy and have problems with the material drying, clinging to surfaces, and clumping, which prevents it from being milled properly. There may also be contamination by grinding media chipping or breakage (Mercurio, 2020).

Research has been done by comparing the yield percentage of calcium titanate by using ball milling and high shear mixer. From Figure 2.2 below, it shows that 10 minutes of high shear mixer, which is the K-1 in figure has achieved similar level of yield percentage compared to 3 hours of ball milling (Mercurio, 2020). High shear, outcome quality of high shear mixing is

substantially equivalent to ball milling in this scenario but needs much shorter mixing durations. This is helpful for these sorts of ceramic systems for a variety of reasons. For example, decreased contamination, higher efficiency, lower energy consumption, and simplified batch planning.
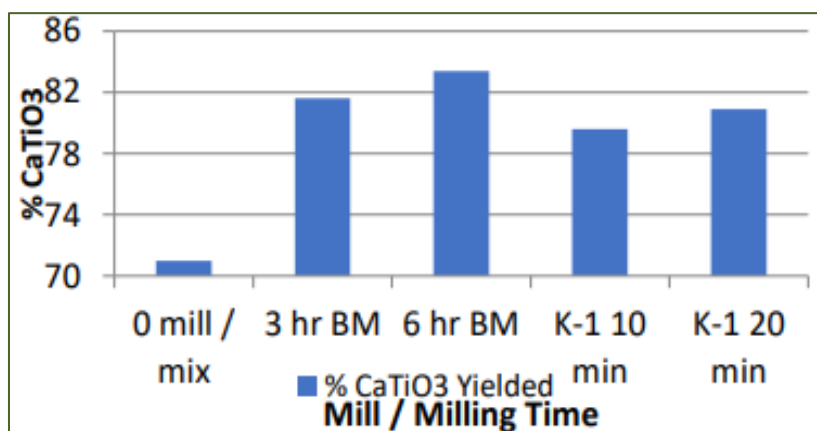
Figure 2.2: Yield Percentage of calcium titanate (Mercurio, 2020).

2.4   Type of binders for ceramic ink

In direct ink writing (DIW), the binder plays a crucial role in controlling the properties of the ink and ensuring successful printing. It manages ink viscosity and rheology for smooth extrusion and shape retention, stabilizes the suspension for consistent print quality, and enhances adhesion and cohesion to create stable structures. Additionally, compatibility with post-processing methods influences the final mechanical and functional properties of printed objects. The ability to customize binders for specific applications allows DIW inks to be tailored for diverse fields such as biomedical engineering and electronics.

The first common type of binder is organic polymers, where cellulose derivatives is one of the best examples. It is including carboxymethyl cellulose (CMC) and cellulose nanofibers (CNFs), are cost-effective and environmentally friendly options (Hadi, et al., 2021). CMC efficiently links active material particles together and provides high viscosity and shear-thinning behaviour. It is used in inks containing lithium iron phosphate and lithium titanate particles for printing Li-ion battery electrodes. Additionally, silver nanowires and carbon nanotubes can be added to CMC inks to improve conductivity. CNFs, a type of nanocellulose rich in hydroxyl groups, promote hydrogen bonding and can be

loaded with active material particles to formulate printable inks. These have been used to print cathodes for Li-metal batteries, which are carbonized after printing (Tagliaferri, Panagiotopoulos and Mattevi, 2020). Besides that, Hydroxypropyl methylcellulose (HPMC) is also one of a common cellulose derivative-based binder used for DIW. HPMC is water-soluble, which facilitates easy mixing with other ink components and allows for fine-tuning of the properties of the ceramic ink to match specific printing requirements. Another study done by Pattaraporn and the teams also found that HPMC exhibited good extrudability and printability, making it suitable for 3D printing applications (Pattaraporn Panraksa, 2020). Generally, cellulose derivatives-based materials offer several advantages over commonly used 3D printing filaments like polylactic acid (PLA) and acrylonitrile butadiene styrene (ABS). These benefits include cost-effectiveness, the ability to print at room temperature, and an eco-friendly production process (Yiliang, et al., 2020).

Other than that, Pluronic is also one of the organic polymer binders. It also known as a triblock copolymer, forms thermoresponsive hydrogels at high concentrations in water. It exhibits thermoresponsive behaviour, changing properties with temperature and forming a gel at higher temperatures to enhance ink stability during printing (Nisar, et al., 2023). For example, Pluronic F-127 also provides rheological control, helping manage ink viscosity and flow properties for desired printability and precision. Pluronic is biocompatible, making it suitable for tissue engineering and biofabrication applications. It is soluble in water and compatible with various polymers and materials, aiding ink formulation. Furthermore, Pluronic stabilizes ceramic particles in the ink, preventing settling and ensuring uniform distribution. Initially developed for ceramic particles, Pluronic is now applied to energy materials as well. Pluronic-based inks offer solid-like behaviour at rest and flow when sheared over the yield point. An experiment is conducted by Belgin, et al. (2023), they found that ceramic ink made by Pluronic F-127 has grater storage and loss modulus than polyvinyl alcohol (PVA) where the result is showed in Figure 2.3.
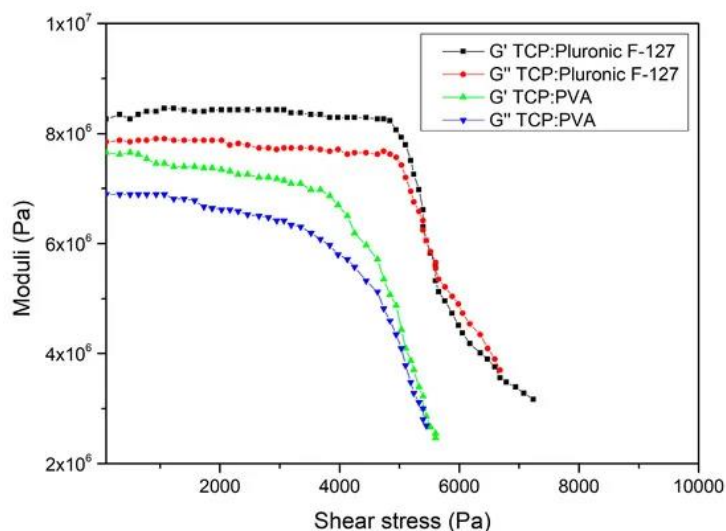
Figure 2.3: Effect of storage and loss moduli of ceramic ink (Belgin, et al. 2023).

Beside organic polymers, there is another type of binder called natural polymers. The Hyaluronic acid (HA) is a natural polymer similar to cellulose, which can serve as an effective binder and rheology modifier in DIW. It enhances the viscosity and flow properties of ceramic inks, aiding printability and shape retention during and after the printing process (Tagliaferri, Panagiotopoulos and Mattevi, 2020). HA is known for its excellent biocompatibility, making it an attractive choice for biofabrication and biomedical applications. HA can absorb and retain water, providing hydration and contributing to ink stability and consistency (Ouriel, 2023).

Generally, the analysis of the types of binders used in DIW for ceramic inks reveals that a range of materials can be employed to achieve desired properties such as printability, stability, and mechanical strength in the final printed structures.

2.5   Type of solvent for ceramic ink

The choice of solvent and its concentration in the ceramic ink can have a significant impact on the printing process, final material properties, and post-processing requirements. The selection of the appropriate solvent depends on factors such as the ceramic material used, the 3D printing technology, and the desired outcome. Different combinations of solvent and binder will create different types of ink, which are having completely different properties. For

example, a low-viscosity liquid, such as water, and a small portion of organic additives were used to form a Colloidal ink. This ink may be relatively sensitive to variations on the chemistry and pH of the environment (Laura and Maria, 2021). Other than that, other mechanical properties of the 3D printed product are also influenced by the chemical solvent utilized.

According to Kharissova and his fellows, water-based solvents are created as an environmentally friendly choice to existing solvents. Using water-based solvents, on the other hand, affords a new set of issues. They need cautious formulation to maintain stable suspensions of Forsterite particles, a mineral often employed in a variety of applications. This stability is critical for ensuring uniform distribution and quality of items such as inks or coatings. These solvents have idiosyncratic drying kinetics, which means they evaporate and solidify uniquely. This peculiarity can cast a shadow over operations such as printing, potentially resulting in complications such as uneven drying or production slowdowns. Despite its eco-friendly allure, the use of water-based solvents necessitates careful study and experience to efficiently negotiate these complexities (Kharissova, et al., 2019).

A study of the influence of density and mechanical properties using several types of chemical solvents is conducted by He, et al. (2020). The research project encompassed the production of a green body composed of alumina ceramic, with photosensitive resins employed as the binding agent. Stereolithography additive manufacturing (AM) technology was utilized for the printing process. Next, a different chemical solvent was used in the solvent debinding stage, where the identical thermal debinding and sintering techniques will be used also. These methods were used to generate a solid 3D printed alumina item. (He, et al., 2020). From the result obtained, the microstructure of the samples altered dramatically following solvent debinding, heat debinding, and sintering, resulting in loose spongy structures, porous aggregates, and compact structures, respectively. However, the magnitude to density and porosity change is not significant. It also states that the application of several types of debinding solvents lowered the flexural strength of the sintered sample by up to 50%, with a high of 63.4 MPa and a minimum of 32.6 MPa. Therefore, the selection of solvent is important to define the mechanical characteristics of printed products.
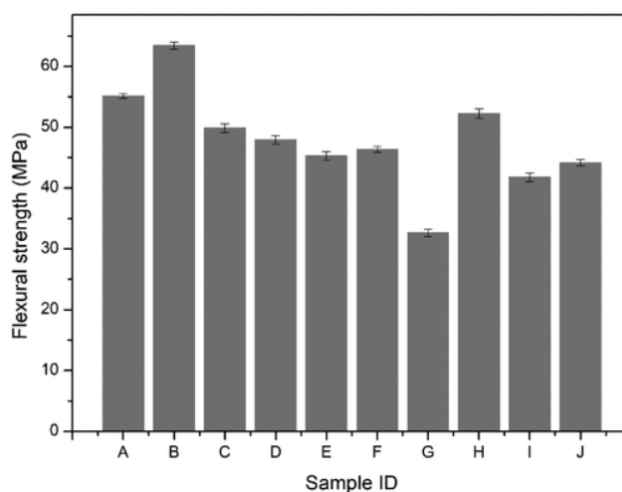
Figure 2.4: Flexural strength of alumina ceramics impregnated in different solvents (He, et al., 2020).

2.6   Organogel Ink

Organogel ink is one of the materials in the field of 3D printing and additive manufacturing. The organogel ink is a type of solvent-based ink, and organic solvent are used as the solvent component (Jisu, et al., 2021). From the research report by Smallwood (1996), the organic solvent can be categorized into few types. First, hydrocarbons such as aliphatic solvents like naphtha, paraffin hydrocarbons including hexane, and aromatic solvents such as benzene, are types of organic compounds. Additionally, alcohols such as methyl alcohol, ketones like acetone, and esters such as ethyl acetate are also significant organic substances, are also prevalent in various industries. Additionally, ethers such as diethyl ether, isopropyl ether, and tetrahydrofuran, are other organic substances commonly used in a variety of applications.

Some of the organic solvents are generally low boiling point and low evaporating point, which is around room temperature. Therefore, in terms of 3D printing, the transition from printed part of organogel ink to green part is shorter. The green part indicates the solvent is evaporated in the printed part. Thus, the process time from printing to sintering is shorten (PrintWiki, 2023).

In the study reported by Leïla, et al. (2021), orgagonel are formed by the self-assembly of low molecular weight organic molecules in a liquid medium, resulting in a gel-like structure that can retain the liquid within a three-

dimensional network. The organic molecules, often called gelators, form a network through non-covalent interactions such as hydrogen bonding, van der Waals forces, or π-π stacking. This network immobilizes the liquid phase, giving the organogel its semi-solid consistency. This also make the organogel ink has generally greater mechanical properties than other inks.

2.7   Rheology analysis

DIW is an extrusion-based technology for printing at room temperature by using a non-Newtonian slurry with high viscosity and composite rheological parameters and a configuration of liquid and solid phases (Aamir and Ismail, 2021). The slurry's capacity to flow through the small nozzles and generate a continuous flow upon exit with uniform cross-sectional area, as well as its ability to dry upon contact with the substrate to keep the shape and form the layer, is one of its most important qualities. One of the most difficult challenges in DIW is producing a high-density item without agglomeration the nozzle. This is only feasible if the particles in the slurry are distributed uniformly. As a result, for the intended prints, the slurry rheology, particle size distribution and morphology, and wetting qualities must be optimised (Laura and Maria, 2021).

Slurry with pronounced non-Newtonian characteristics is favoured for 3D printing, particularly those exhibiting significant shear thinning at high shear rates. This behaviour ensures a smooth extrusion process by maintaining low viscosity during nozzle flow at high shear rates and a rapid viscosity increase as the material exits the nozzle, preventing dripping. Additionally, the presence of a yield stress component is preferred as it guarantees shape stability of the filament in the stand-off region and during deposition. However, while non-Newtonian features promote extrudate swelling, careful process optimization is necessary to prevent shape distortions (Rossella and Alberto, 2022). According to another research, it also states that the feedstock used in FDM technology should exhibit shear-thinning behaviour. This is due to this behaviour allowed the feedstock to be extruded through the nozzle with low piston extrusion force, as the viscosity gradually decreases when subjected to small increases in shear rate (Huang, et al., 2021).

The shear thinning behaviour is studied with a test of ceramic ink of 50 vol% solid loadings of alumina with 0.4 wt% carrageenans as an additive. From

Figure 2.4, as the shear rate of ceramic ink increases, its viscosity decreases. And the shear stress is also increased to maintain that shear rate increases (Aamir and Ismail, 2021). This behaviour is also proved by the flow sweep test of 30 wt.% Pluronic F127 hydrogel and the same hydrogel loaded with 50 wt.% of β-TCP particles (Laura and Maria, 2021). The viscosity decreases as the shear rate increases. This phenomenon is commonly noticed in everyday products like paints. When these products are at rest, their viscosity is significantly higher compared to when they are spread on a surface, which involves a high shear rate. This change occurs due to the disruption of internal interactions within the fluid or the rearrangement of molecules or particles in the direction of the flow, transitioning from an initial disordered state when not in motion.
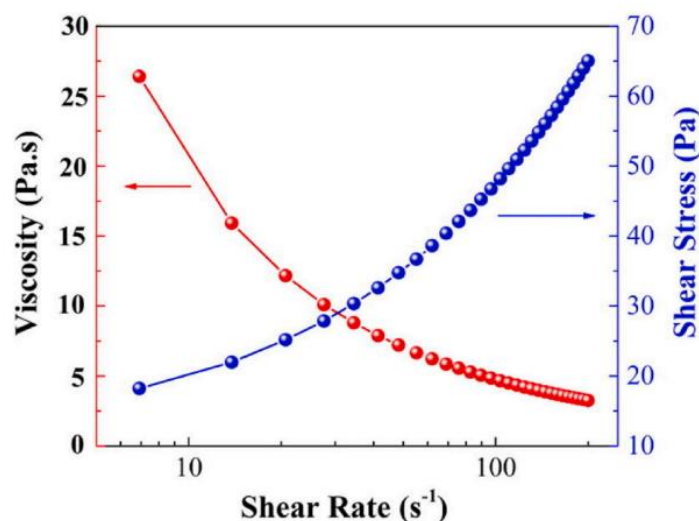
Figure 2.5: Shear stress vs Viscosity vs the shear rate of the slurry (Aamir and Ismail, 2021).

Other than the behaviour of shear rate and viscosity, the relationship between G' and G'' vs shear strain is also studied by Amplitude sweep test which shown in Figure 2.5. In this context, G' is the storage modulus, and G'' is the loss modulus. When G' is greater than G", the elastic behaviour continues to outperform the viscous, but the yield stress has been overcome, indicating a solid-like behaviour with irreversible deformation. However, when G' is equal to G'' represents the transition from solid-like to liquid-like behaviour. When G' is less than G'', it means the material has a liquid-like behaviour. The

amplitude sweep tests can indeed help in determining optimal values for various rheological parameters, such as elastic modulus, yield stress, and flow stress, in the context of assessing the printability of ceramic ink (Laura and Maria, 2021).
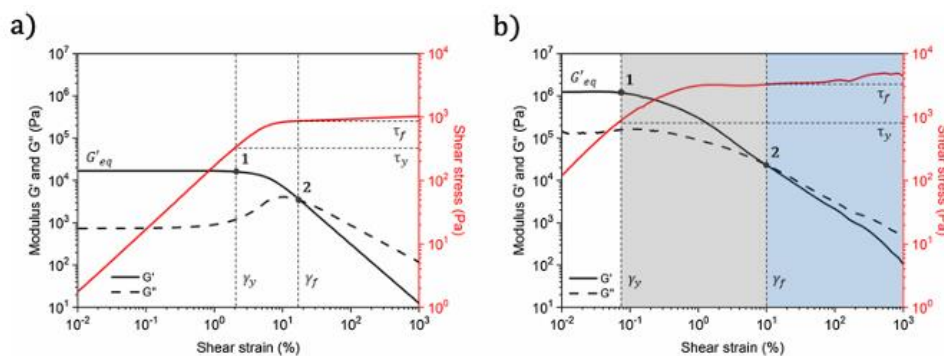
Figure 2.6: Amplitude sweep test at a frequency of 1 Hz of a 30 wt.% Pluronic F127 hydrogel (a) and the same hydrogel loaded with 70 wt.% of β-TCP particles (b) Tests carried out at 23 C, using a 20 mm rough parallel plate geometry with a 500 μm gap and a solvent trap (Laura and Maria, 2021).

The three-interval thixotropy test (3ITT) serves as a valuable rheological assessment, particularly in emulating the behaviour of materials during extrusion-based printing. This test involves three sequential phases with varying shear rates, which shown in Figure 2.5. First, a low shear rate within the linear viscoelastic range. Secondly, Strong shear to simulate structural breakdown of the sample during the coating process at a preset high shear rate. Lastly, a low shear rate once again emulates the ink's post-deposition resting state. In DIW, the recovery process needs to be sufficiently rapid to ensure precise shape accuracy and prevent the structure from slumping. It's important to recognize that the ink is not fully stable when it exits the nozzle. (Tagliaferri, Panagiotopoulos and Mattevi, 2020). This assessment is based on the examination of shear moduli recovery, spanning from maximum to minimum shear rates (Pascal, et al., 2022).
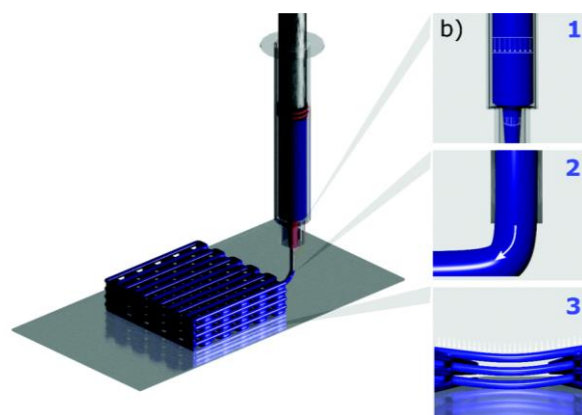
Figure 2.7: Phases during printing for 3ITT (Tagliaferri, Panagiotopoulos and
　　　　　 Mattevi, 2020)

Rotational or shear rheometers represent precise instruments employed for subjecting a sample to a broad spectrum of shear stresses, strains, and rates. This is achieved using distinct geometric configurations and meticulous control over environmental conditions. The most frequently utilized configurations include concentric cylinders, cone-plates, and parallel plates, where the upper component is mobile while the lower component remains stationary. For highly viscous materials, such as the ceramic pastes utilized in direct ink writing (DIW), the parallel plate configuration is particularly well-suited. It is essential to adjust the gap between the plates, with a recommended minimum size that should be at least ten times greater than the largest particles present in the sample (Laura and Maria, 2021). These rheometers enable testing in either rotational or oscillatory modes, with the latter being commonly referred to as dynamic testing. In the rotational mode, the upper component maintains continuous rotation in one direction, whereas in oscillatory mode, it undergoes sinusoidal oscillations at specific amplitudes and frequencies (Hochstein, n.d.).

2.8　　　Ceramic porous structures

The fabrication of porous structures with biological, material engineering, and aesthetic relevance is one of the emerging application areas of 3D printing, and design for 3D printing of porous structures has become a significant research subject (Sharif, et al., 2020). Biological structures are frequently used as inspiration for the development of high-performance mechanical structures due to their mechanical properties. Nonetheless, typical manufacturing techniques

are sometimes incapable of accurately recreating the complicated and delicate character of biological systems. Modern additive manufacturing techniques enable the development of materials with complex designs inspired by biological processes (Shakib, et al., 2022).

Research conducted by Barry and his fellows, according to the researchers Porosity, a controlled property of 3D-printed items made from Phyllosilicate-Based ceramic ink, is a critical component with far-reaching uses such as filtration, catalysis, and structural strength. This porous property, similar to latent potential, opens up a world of possibilities. Tailored pore sizes and distributions enable exact material flow in the field of filtration. In catalysis, the increased surface area of porous materials increases reactivity. Even in terms of structural integrity, the strategic use of porosity, which is influenced by variables like layer thickness and infill density, results in materials that are both tough and lightweight. The interaction between printing settings and porosity serves as an example. The layer thickness and infill density are not chosen at random, but rather as a deliberate decision driven by the desired porosity and, thus, the intended use of the printed product. This also known as macro porosity. The interaction of parameters and porosity impacts the final properties and usefulness of 3D-printed items (Barry, et al., 2022)
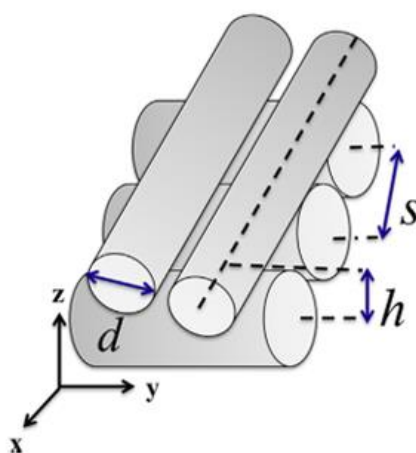
Figure 2.8: Dimension for macro porosity calculation of the scaffolds (Catarina, et al., 2016).

There are two common types of porosity in the DIW, which are micro porosity and micro porosity. The macro porosity in DIW is mentioned in last paragraph, as it is a pre-designed porosity from geometrical consideration with the parameters of span length, layer-to-layer height, filament width and volume of cylinder intersection, which shown in Figure 2.6. However, the value v_i can be neglected if small layer overlaps, which is less than 20% since it is well below 1% of the total volume of the structure (Catarina, et al., 2016).

$$P_{macro} = 1 - \frac{2\pi(\frac{d}{2})^2 s - v_i}{2d(\frac{h}{d})s^2} \tag{2.4}$$

Where

s = Span length (mm)

h = Layer-to-layer height (mm)

d = Filament width (mm)

v_i = Volume of cylinder intersection (mm^3)

However, if the v_i is less than 20%, a simplified version of formula can be used.

$$P_{macro} = 1 - \frac{\pi d}{4(\frac{h}{d})s} \tag{2.5}$$

In other hand, micro porosity is can form during the material's creation or processing, such as during the sintering of ceramics or other materials, where the packing of particles can leave behind very small gaps. They can also arise from the molecular structure of polymers or other materials (Pecqueux, et al., 2010). Micro porosity can be calculated by equation (2.6).

$$P_{micro} = \left(1 - \frac{\rho_b}{\rho_{th}}\right) \times 100\% \tag{2.6}$$

Where

ρ_{th} = Theoretical / true density of the sample (g/cm^3)

ρ_b = Bulk density of the sample (g/cm^3)

In DIW, micro porosity can further categorize into two types, which are apparent porosity and closed porosity. Generally, apparent porosity is the measure of the total volume of interconnected or open pores within a material, and these pores allow fluid to flow in and out of the structure. Apparent porosity, P_a normally can be determined by Archimedean method, which measure the mass of object in different conditions (Kai, et al., 2020).

$$P_a = \frac{m_3 - m_1}{m_3 - m_2} \times 100\% \qquad (2.7)$$

where

m_1 = Dry mass of the sample (g)

m_2 = Saturated mass of the sample in the suspension (g)

m_3 = Saturated mass of the sample in air after immersed into water (g)

The closed porosity, P_t is the measure of the volume of pores within a material that are isolated from the surface and from each other. These pores are not accessible to fluids from the outside (Coleman and Beeré, 1975). Closed porosity is typically measured using technique of light scattering (static and dynamic), small angle x-ray scattering (SAXS), and small angle neutron scattering (SANS) (Espinal, 2012). It can also be calculated by using density and apparent porosity (Kai, et al., 2020).

$$P_t = \frac{\rho_{th} - \rho_b}{\rho_t} \times 100\% - P_a \qquad (2.8)$$

$$P_t = P_{micro} - P_a \qquad (2.9)$$

Where

ρ_{th} = Theoretical / true density of the sample (g/cm^3)

ρ_b = Bulk density of the sample (g/cm^3)

An experiment is conducted by Pecqueux, et al. (2010) to study the relationship between micro porosity and macro porosity on the mechanical properties. In general, for both micro porosity and macro porosity, as porosity

increases in a material, mechanical properties such as Young's modulus, toughness, and compressive strength tend to decrease. This is due to pores and voids act as stress concentrators and weak points within the material, leading to earlier initiation of fractures and a reduction in the material's ability to bear loads. Controlling porosity is crucial for optimizing mechanical performance of materials in various applications.
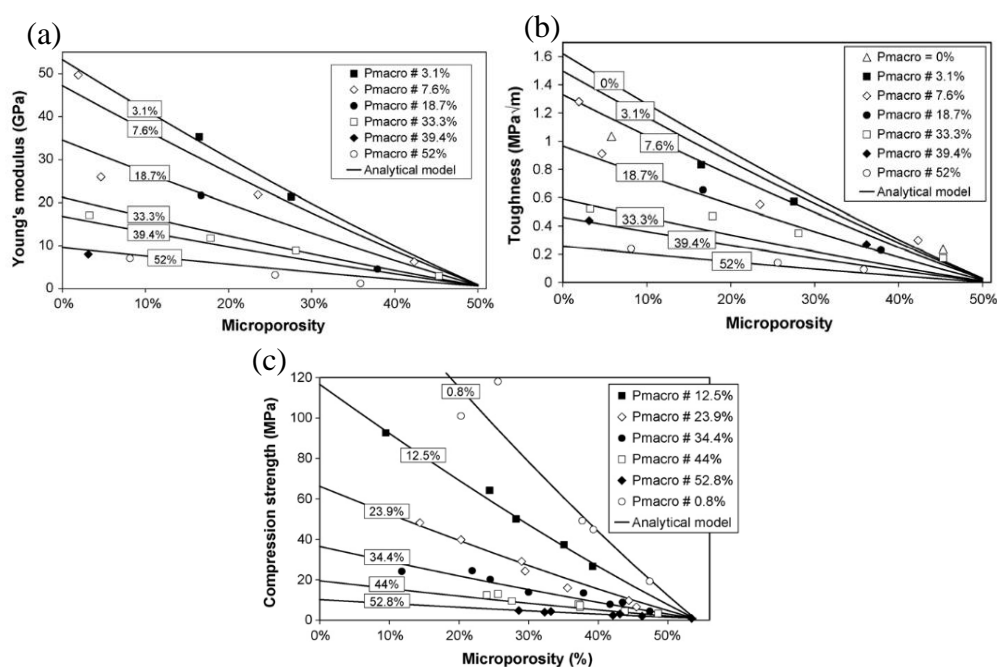
Figure 2.9: (a) Young's modulus, (b) toughness and (c) compressive strength as function of microporosity, for different microporosities (Pecqueux, et al., 2010).

In addition, to prevent the separation of powders during the mixing process, it is common practice to incorporate binders into the mixture. These binders create granular materials in which space holder particles are coated with smaller metal matrix particles. Ideally, these binders should be in liquid form and should completely evaporate during the sintering process (Francisco, et al., 2022). Therefore, the modification of weight percentage of binder is important to control the porosity of printed products (Budi and Jie, 2014).

Other than adjusting the ratio of binder and solid powder, highly porous materials using 3D printing can also be produced by integrating the innovative 3D-Painting method with conventional salt-leaching techniques. As an illustration, when employing salt-based ink like $CuSo_4$, the printed object

undergoes a simple washing procedure using aqueous solutions to dissolve and eliminate the salt constituents from the 3D-printed framework. This washing process leaves behind a highly porous elastomeric polymer framework, which is medical-grade polylactic-co-glycolic acid (PLGA) in this case. Importantly, this process of salt removal maintains the 3D-printed architecture, ensuring that the structural integrity of the printed object is preserved (Jakus, Geisendorfer and Lewis, 2018). Therefore, the combination of specific salt chemistries along with a particular sequence of washing and leaching steps, results in a further increase in the total porosity of the final product. This indicates the ability to control and enhance the porosity of the 3D-printed material using this method.

2.9   Summary

In summary, AM technology creates a three-dimensional object layer by layer, controlled by a 3D printer. The application of additive manufacturing is become widely accepted by many industries. As it provides better accuracy, material diversity, efficiency and cost effective.

In this project, the integration of forsterite as ceramic ink in 3D printing is studied. Due to its low dielectric loss regarding extremely high-frequency electromagnetic waves, forsterite ceramics are employed as a dielectric material in high-frequency circuits such as submillimetre-wave applications. Forsterite has utilised in electronics, communication, and refractory field. With its high melting point and low thermal conductivity, it also suitable to use in construction field. These properties of forsterite are because of its unique crystal structure. To synthesise the forsterite, chemical structure and formula (Mg_2SiO_4) is studied. The material to produce forsterite is categorized into two group, which is magnesium source and silica source. The material is studied from the aspect of particle size and reaction step. This is to minimize the contamination for final product and ensure the quality of forsterite. While two methods to synthesis forsterite is studied, which is ball milling and high shear mixer. Ball milling is the method that use steel or ceramic ball as the milling media. By revolving the container, collisions and friction between balls and material will break and reduce size. However, from the research, the time for ball milling has no direct effect to the crystallite size, which means that there is a peak for the performance of ball milling. For high shear mixer, it offers some advantages

over ball milling. For example, the process time of high shear mixer is shorter than ball milling, high shear mixer also reduces the possibility of contamination such as breakage of milling media.

For the formulation of ceramic ink, the type of solvent is one of the crucial materials. Different types of solvent will produce different types of ink, where all inks have significant different properties. For example, chemical resistance and mechanical properties such as flexural strength. With the organic solvent, organogel ink will be produced, which has better mechanical properties than other type of ink. To optimize the printing experience, the rheology of the ceramic ink should be stressed. Rheology of ink not only defines the ability to flow through nozzle, but also ensures that no clogging happens at the nozzle. The shear thinning behavior of ink is benefit to 3D printers. It ensures the smoothness of the extrusion during printing. After that, to create a porous structure for the application of biological and material engineering, the weight percentage of binder in the ceramic ink is required to adjust. Other than binder, there are also another method by using the property of salt. It creates porous structure by remove the salt component in salted-based ink, this can be done by washing and leaching. Other than that, the macro porosity can also be produced by designing the printing parameters such as layer width, layer-to-layer height and span length.

CHAPTER 3

METHODOLOGY AND WORK PLAN

3.1   Introduction

This chapter was discussed about the procedure from synthesis of forsterite until sintering of 3D printed product. In this project, the forsterite powder was first prepared using hydrophilic fumed SiO_2 and MgO. Then, XRD analysis will be perform to analysis of the crystal structure and properties of materials. After that, several sets of formulation were preparing to optimize best material and ratio for the formulation of ceramic ink. Then, prepared ceramic inks were performed printing by 3D printer and undergo debinding and sintering. The ceramic inks were also performed rheology analysis to study the behaviour of the ceramic ink. Lastly, the printed samples were performed physical properties test such as density test and hardness test. This chapter also described the hypothesis development and different formulation used to product the forsterite ceramic ink with the aim of porous structure.
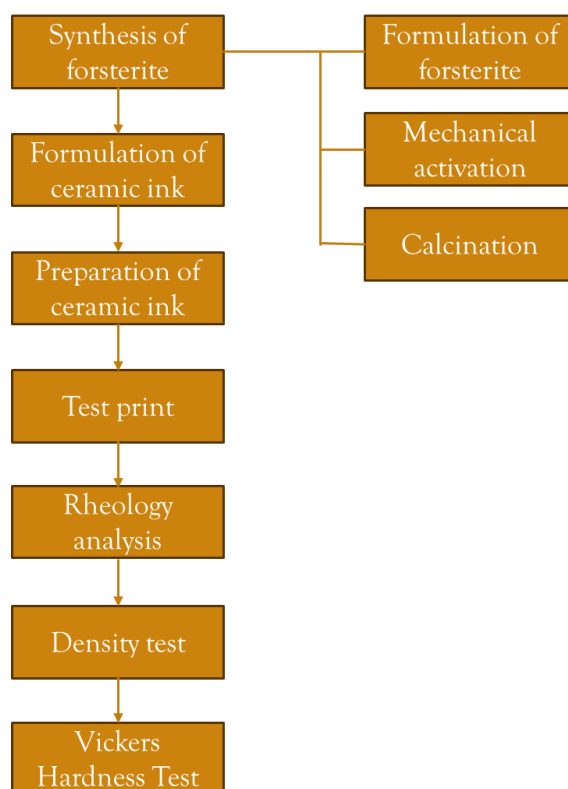

Figure 3.1: Process of the project

3.2   Synthesis of forsterite

The process of synthesis of forsterite includes determination of ratio and amount of MgO and hydrophilic fume SiO_2. This can be calculated by the molecular weight for every chemical element. For the record, molecular weight for Mg is 24.3 g/mol, O is 16 g/mol, Si is 28.1 g/mol and H is 1 g/mol. With this information, the molecular weight of MgO, SiO_2 and forsterite can be calculated. And the calculated molecular weight of MgO was 40.3g/mol, SiO_2 was 60.1g/mol and forsterite was 140.7 g/mol.

$$MgO = (24.3 + 16)g/mol = 40.3g/mol \qquad (3.1)$$

Then, a balance equation was formed to determine the number of moles for every substance. By fixing the desire mass of forsterite powder, number of moles of forsterite was able to be calculated by simple divide the total mass by its molecular weight. From Equation (3.2), which shown that SiO_2 has the same number of moles with forsterite. However, the number of moles of MgO was twice that of forsterite. After the number of moles for both substances were obtained, the mass required can be calculated by dividing with the molecular mass. As a side note, the actual mass for SiO_2 was set to have additional 1.5%. This was due to the consideration of lost during furnace and along the process of forsterite synthesis, as hydrophilic fume SiO_2 was a very lightweight powder with very small particle size. Thus, if the total desire forsterite powder was 100 g, the actual mass required for SiO_2 was 43.36 g, and 57.29 for MgO.

$$SiO_2 + 2MgO \rightarrow Mg_2SiO_4 \qquad (3.2)$$
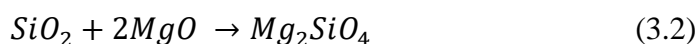
3.2.1   Mechanical activation by high-shear mixer

Before the measurement of reactants, the mixing shaft and 2 mixing blades of high shear mixer were assembled. Then, the mixer was started with low rotational speed to check if there was any knocking sound between components or high amplitude of shaking. This indicates that not concentric of assembled components. Therefore, the components should reassemble if the knocking sound or vigorously shaking appear.

Then, the hydrophilic fume SiO_2 was first measured into the correct amount and transfer to the large jug. It should notice that the measurement and transfer of hydrophilic fume SiO_2 was repeated several times with small amount each time to increase the accuracy. This was due to the sensitivity of electron beam might affect if too much of hydrophilic fume SiO_2 was measured at the same time. The lightweight nature of hydrophilic fume SiO_2 allows it to have a greater volumetric capacity than other materials at constant mass. After all hydrophilic fume SiO_2 was transferred into jug, 500 ml of deionized water was added as the milling medium. The jug with deionized water and hydrophilic fume SiO_2 was then placed under mixer. The mixer was then adjusted to ensure the mixing process was able to reach until the bottom of jug. The location of upper blade was also adjusted to a suitable level to create the vortex during the process. The upper blade should be placed slightly lower than the water level. Then, mixing process was initiated by low rotational speed of 2000 rpm.

While the mixing of hydrophilic fume SiO_2 was processing, MgO was measured for the next step. After that, the mixer was stopped before MgO was added to the mixture. The mixing process was then continued by 4500 rpm for 2 hours. Ethanol (95%) was used to flush the mixing components and circumference of jug throughout the mixing process to prevent the mixture sticks on the wall of the jar and mixing part. The temperature of mixer and mixture were monitored to prevent overheat. Deionized water or ethanol may add by observing the viscosity mixture and suction condition during mixing. The mixture was then transferred to bowl after 2 hours mix. The oven was preheated at the constant temperature of 90 °C before the bowl with mixture was placed into it. The duration of oven drying takes at least 5 hours. However, the actual duration was depended on the volume of mixture and amount of deionized water added.

Figure 3.2: High-shear mixer.

3.2.2   Calcination

To perform calcination of forsterite powder, the mixture after oven dry process was collected into a mortar. Then, the dried mixture was grinded by using mortar dan pestle to a powder form. This was for the purpose to increase the efficiency of calcination. For the calcination process, the sample was heated to 1200 °C, at a heating rate of 10 °C/min for 2 hours. A holding time of 3 hours was maintained at the desired temperature to carry out the crystallization process. Finally, the sample was ground and sieved to a fine powder, and the mass was measured.
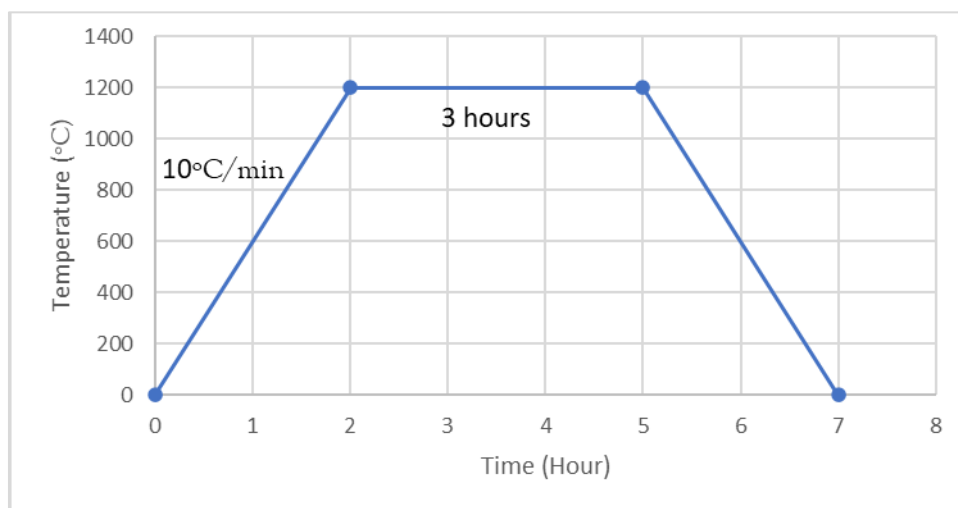

Figure 3.3: Temperature profile of calcination

3.3 X-ray Diffraction analysis

A small portion of the furnaced forsterite powder was collected for XRD analysis to study the crystal structure of the specimens and determine the purity of the sample. The scan range was set to be 10º- 60º, with the scan speed of 2º/minute. This was due to XRD can identify the different crystalline phases present in a sample. If the sample was pure, it should exhibit diffraction peaks corresponding to a single phase. If impurities or additional phases were presented, additional diffraction peaks from those phases could be detected. By analysing the diffraction pattern, the purity of the sample was able to be determined.

After collected the XRD result, the peak list graph was used in HighScore Plus to determine the purity of sample. The graph of intensity against 2θ was also plotted by using OriginPro to have a better visualization.

3.4 Formulation of ceramic ink

The formulation of ceramic ink required the study of material and ratio for solid loading, binder, solvent, dispersant, and others. In this study, the ink formulation was prepared based on the research reported by Ang, Tey and Yeo (2024). After the analysis of printability, rheology behaviour and mechanical properties, the optimum formulation for slurry was 45 vol% solid content, 300 g/L binder concentration, and 1 vol% defoamer. Due to the planned use of a similar type of binder and solvent, specifically the cellulose derivative binder (CDB) with the code SLB-100 from Solid Lab and acetone as the solvent, these values were used as the initial formulation parameters. Other than that, to improve the performance of the ink and the quality of the printed structures, Diethy Phthalate was added as plasticiser to improve the flexibility of filament and provide better layer-to-layer adhesion, and BYK 110 was added as dispersant to help to evenly distribute solid particles throughout the ink, preventing clumping or agglomeration. From initial values, several sets of formulation were prepared to obtain the optimum formulation.

Table 3.1: Composition of ceramic ink formulation.

Sample	Forsterite , vol%	CDB (Binder) , g/L	Binder Solution , vol%	Plasticiser , vol%	Dispersant , vol%
1	35	300	40	15	10
2	35	400	40	15	10
3	40	300	35	15	10
4	40	400	35	15	10
5	43	300	32	15	10
6	43	400	32	15	10
7	45	300	30	15	10

3.5 Planetary centrifugal mixer for ceramic ink preparation

The ceramic ink was prepared by using planetary centrifugal mixer. A planetary centrifugal mixer works by rotating and circling a mixing container at the same time, creating centrifugal forces that encourage thorough and uniform mixing of ingredients while also offering vacuum degassing capabilities.

3.5.1 Fabrication of container fitting

In the formula of ceramic ink in this project, acetone was used as one of the solvents. Due to the properties of acetone, the original container used for planetary centrifugal mixer will be damage if contract with acetone for a long period of time. Therefore, another pair of containers were used for the preparation of forsterite ink in this project. However, due to the difference of size, the new containers were not able to fit with the original fitting of mixer. Hence, a special fitting was required to fabricate for these containers. Due to the fitting of planetary centrifugal mixer was required to be lightweight and accurate dimensions, 3D printing was used as the fabrication method for the fitting.

First, the dimensions of container and fitting socket of mixer were taken, which were outer diameter of container, inner diameter, and depth of socket. Then, the 3D model of the fitting was drawn and modified in SolidWorks

with correct dimensions which shown in Figure 3.4. The g-code of model was generated by using the slicing software and transfer to the printer. Then, the 3D printing was performed by using PLA as the material. Finally, the printed product was tested with the mixer and performed surface finishing.
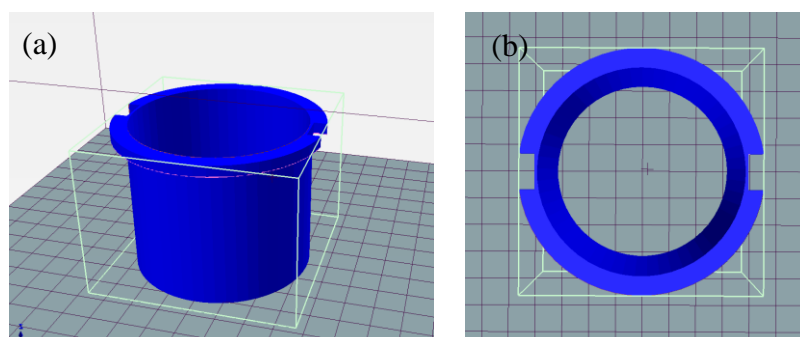

Figure 3.4: 3D model of container fitting in (a)isometric view and (b)top view

3.5.2   Preparation of ceramic ink

Prior to initiating the planetary centrifugal mixer, careful attention was given to the fitting of the container. It was important to ensure that the mass difference between both sides of the mixer did not exceed 15 g and was kept as low as possible for balanced rotation. The timer was set for 1 minute, and the speed was adjusted to 2000 rpm. The green button was then pushed to start the mixing process. Power was switched off when removing the container.

Figure 3.5: (a) Planetary centrifugal mixer (b) internal mixing chamber

The preparation of ceramic ink was first started with the measurement of initial weight of the mixer container, followed by the addition of dispersant

and plasticiser. Subsequently, acetone was added into the container, and its current weight of container with mixture was recorded. Then, the container with the mixed components was securely covered.

The container with acetone, dispersant and plasticiser were performed the first mixing in planetary centrifugal mixer. Then, the forsterite powder was added to the mixture along with 10 ceramic balls. The purpose of ceramic balls was to improve the homogeneity of mixing result, which similar to the concept of ball milling. The mixture was then performed second mixing process in planetary centrifugal mixer. After that, the container along with the mixer was cooled down in water bath for 15 minutes. This allowed the forsterite to fully disperse in the mixture and helps reduce the evaporation rate of acetone caused by heat generated during mixing.

Figure 3.6: Mixture with ceramic ball

Lastly, the cellulose derivative binder (CDB) was added to the mixture and perform mixing in planetary centrifugal mixer. Then, the 10 ceramic balls were taken out by using tweezer, and the mixture was then sent to perform the last mixing. After mixing, the homogeneity of ceramic ink was checked, and if needed, the mixing of planetary centrifugal mix may be repeated for another time. The latest weight of the mixture with container was documented, and the mixture was carefully transferred into a syringe before being inverted for further application. The measurement of weight difference at the starting and ending for mixing was to determine the actual evaporation rate of acetone in the environment of laboratory.

3.6   Test print of ceramic ink

The test print of ceramic ink was performed by using 3D printer, where controlled by g-code. In this project, the g-code was formed by using software of FullControl GCode Designer (FullControl, 2024). The reason of used FullControl GCode Designer to generate g-code instead of slicer software was due to FullControl GCode allows users to have precise control over various printing parameters. They can customize settings that may not be easily accessible through slicer software, such as extrusion unit, bed temperature, layer height and layer width. This level of control was valuable for optimizing print quality and printer performance. When diagnosing and troubleshooting issues with a 3D printer, users may edit g-code directly to test and pinpoint problems. This approach was useful for identifying issues related to specific moves or commands within a print.

Before code for the object, priming sequence was the first code in the software. Allow the printer initiates a priming sequence to ensure the smooth operation of the printing process. This sequence serves multiple purposes, starting with the priming of the extruder nozzle to ensure proper material flow and remove any residue. Simultaneously, it checks the levelling of the print bed to ensure uniform adhesion and quality throughout the print. Additionally, the priming sequence establishes a reference point for accurate positioning and alignment of subsequent layers and features of the main object. By addressing these critical aspects before printing the main object, the priming sequence contributes to the overall success and quality of the 3D print.

Then, the g-code of object can be coded by using the feature of "Line" "Rectangle", "Cartesian repeat", "Line equation polar", "Circle/arc", "Polygon" and others. In this project, 3 models were prepared to analyse different aspects. For example, the square thin wall which was prepared to examinate shape fidelity and determine slumping effect of different ceramic ink. Then, scaffold structure was prepared to determine the sagging effect and study the relationship between macro porosity and micro porosity. Lastly, the solid model was prepared to perform XRD analysis, density test and hardness test. The coding of thin wall and scaffold models was mainly completed with "Line (cartesian)",

"Rectangle" and "Cartesian repeat" features. The G-code of solid was prepared by using slicer software
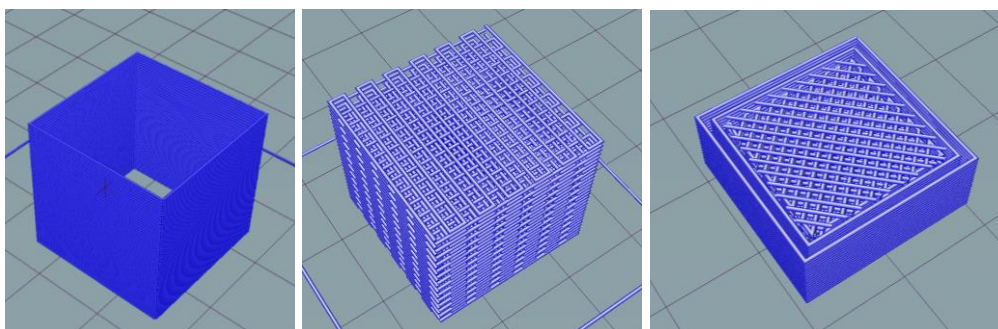

Figure 3.7: Simulated print review of g-code of (a) square thin wall model (b) scaffold structure model (c) solid model

After that, the detail printing parameters were adjusted. The layer width should approximate of the nozzle diameter. Hence, the layer width should around 1.2 mm. And the layer height commonly used was 70-80% of the nozzle diameter. Therefore, for a 16G nozzle of 1.2 mm diameter, the layer height should in the range of 0.84mm to 0.96mm. However, to ensure better finishing for thin wall and solid structure, the layer height was set around 0.4 mm for the printing of thin wall and solid structure. The example of FullControl GCode of thin wall and scaffold models were shown in Appendix B.

Table 3.2: Printing parameters of different models

Model	Layer Height, mm	Layer Width, mm	Print Speed, mm/min	Nozzle Inner Diameter, mm
Thin wall	0.5	1.2	400	1.2
Scaffold	0.8	1.2	400	1.2
Solid	0.5	1.2	300	1.2

3.6.1 Debinding

Debinding was a process in which the green part undergoes the removal of the binder material, resulting in a brown part. If the temperature rises too quickly, trapped gases can cause internal pressure, leading to defects such as cracking or warping in the part. Therefore, to prevent defects and cracking of the specimen, the debinding process was conducted by programmable furnace with heating rate of 2 °C per minute. This was due to programmable furnace can control the heating and cooling rate precisely. After that, the temperature was heat up to 250 °C and holding time of 2 hours. Then, the specimen was cooled down with 2 °C per minute until the brown part form. Figure 3.8 shows the debinding profile of this project.
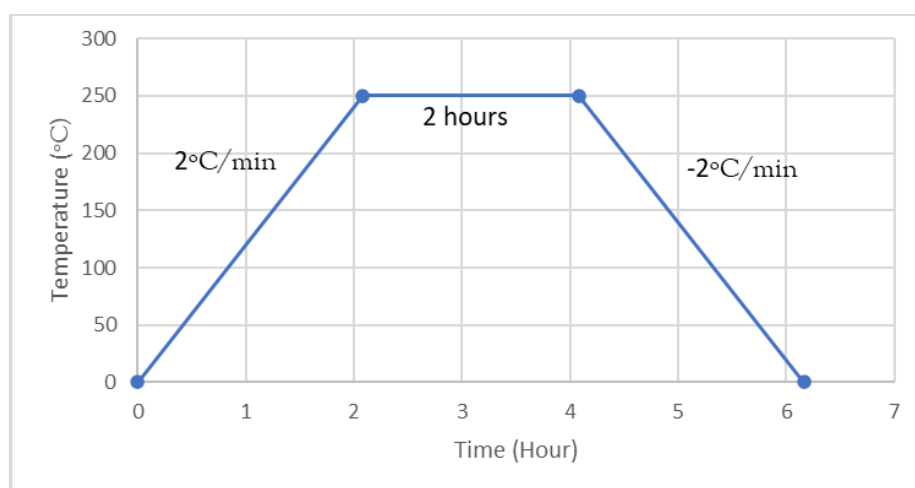

Figure 3.8: Temperature profile of debinding process.

3.6.2 Sintering

In sintering process, the forsterite particle fused together. Therefore, it strengthened the interparticle bonding and removed the remaining binder. The specimens were placed into a sintering furnace with a higher maximum operational temperature. They were then gradually heated to the sintering temperature at 1500 °C, with a controlled heating rate of 5 °C per minute. Once the desired sintering temperature was reached, the specimens were held at that temperature for a duration of 2 hours to facilitate the sintering process. Subsequently, the specimens were allowed to cool down to room temperature

and the mass of the specimens was determined. Figure 3.9 shows the sintering profile of this project.
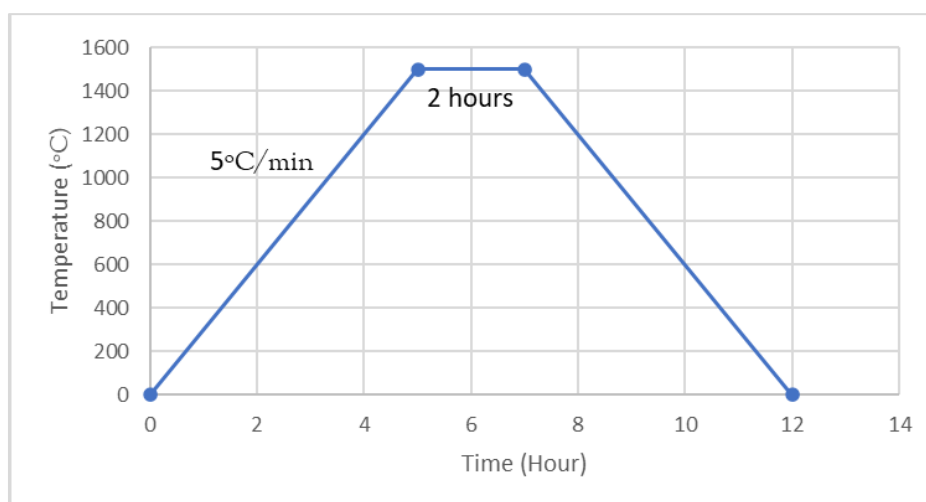

Figure 3.9: Temperature profile of sintering process.

3.7 Rheology analysis

The evaluation of the rheological characteristics, specifically viscosity and linear viscoelastic range, of the ceramic ink was conducted using Anton Paar Rheometer (Physica MCR 301) and the Anton Paar Rheocompass software. To maintain consistency, stainless-steel parallel plate with 25 mm radius was used of all rheology test. After the parallel plate was installed to the rheometer, initial calibration of sensor force was performed by set zero gap between parallel plate and platform. After that, the ceramic ink was carefully positioned at the centre of the rheometer's bottom plate. Then, stainless-steel parallel plate with 1 mm gap between the platform was employed. It's essential to stress the significance of adding a suitable quantity of ceramic ink to prevent underfilling or overfilling, which could compromise the accuracy of the results. Any excess ceramic ink was trimmed to achieve the required load, ensuring that the rheology test was prepared for execution. After the analysis completed, the platform and parallel plate was wiped clean before continuing to next analysis, this was to ensure the accuracy of result and prolong the lifespan of machine.
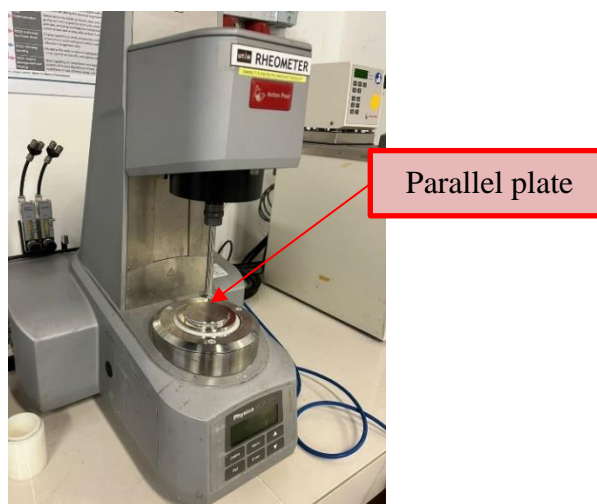
Figure 3.10: Rheometer with parallel plate

The Flow Sweep Test was performed by adjusting the shear rate and evaluating the sample's viscosity at a constant temperature. The shear rate was varied while the viscosity of sample was measured, where the shear rate was set between the range of 0.01 s^{-1} to 100 s^{-1}. Then, the graph of viscosity versus shear rate was plotted. Other than that, the amplitude sweep test was conducted to determine the static yield stress of the ink, with the shear strain range set between 0.0001% and 10% and a constant frequency of 1 Hz. A frequency sweep was also performed to observe changes in storage and loss moduli and the damping factor over a frequency range of 1 to 100 Hz, which was below the yield point. Additionally, the 3ITT test measures the quick recovery of the elastic behaviour of the prepared ceramic ink to ensure the part maintains good shape fidelity. This was done under a constant frequency of 1 Hz, with a shear strain range from 0.01% to 1%. The time intervals vary between 120 and 300 seconds, and the number of data points per interval ranges from 30 to 100 across three intervals in total. It was noted that zero waiting time was implemented in all tests because the high evaporation rate of acetone in ceramic ink could affect the results if exposed to air for too long.

3.8   Density test

The water immersion test was used to determine the density of the sample. Start by measuring and recording the mass of the dry sample using a scale. Next, fill a measuring cylinder with a known volume of water, such as 100 mL, and gently

submerge the sample into the cylinder, ensuring it was fully immersed without any spillage. Measure and record the resulting change in the water level (ΔV), which signifies the volume of the sample. Then, the total density of sample can be calculated by Equation (3.3).

$$\rho(density) = \frac{Mass}{Volume}$$ (3.3)

Other than this, there were another method to determine the density of sample more accurately, which was the Archimedes method. To determine the density of an object using the Archimedes' method, start by weighing the object in air to obtain its dry weight (m_{air}). Then, the object fully immersed in a water of known density and measure its buoyant weight (m_{water}) while submerged. The buoyant weight was the apparent weight of the object in the water. By applying Archimedes' principle, which states that the buoyant force equals the weight of the displaced liquid, the density (ρ) of the object was calculated using the Equation (3.4).

$$\rho(density) = \frac{m_{air}\rho_{water}}{m_{air}-m_{water}}$$ (3.4)

Where

m_{air} = Weight of dry object in air

m_{water} = Weight of object submerged in water

$m_{air-water}$ = Weight of object in air after submerged in water

ρ_{water} = Density of water

Figure 3.11: Apparatus setup for Archimedes' method.

After that, to study the relationship between porosity and the physical properties. The total micro porosity (P), apparent porosity (P_a) and closed porosity (P_t) of samples were calculated by using Equation (2.6) to (2.9). Apparent porosity referred to the volume of open, interconnected pores within a material, which could absorb fluids, while closed porosity referred to the volume of sealed, isolated pores that did not allow fluid penetration and were completely enclosed within the material.

3.9 Vickers Hardness Test

The Vickers hardness test was conducted using a Vickers hardness tester equipped with a diamond indenter. After that, a load of 10 kgf was applied for 10 seconds, and the indentation area was measured. The Vickers hardness value was recorded based on the depth of the indentation. Each sample was tested three times to ensure result accuracy. The Vickers hardness values were converted to SI unit (GPa). The unit HV was actually kgf/mm^2.

$$1 \, Newton = \frac{1}{Gravitational \, Force(9.807N)} \, kgf \tag{3.5}$$

$$Hardness(Pa) = Hardness \left(\frac{kgf}{mm^2}\right) \times \frac{9.807N}{1kgf} \times \frac{10^6 mm^2}{1m^2} \tag{3.6}$$

$$Hardness \, (GPa) = Hardness(HV) \times (9.807 \times 10^{-3}) \tag{3.7}$$

3.10 Optical Microscope

The optical microscope pared with software ZY was used to capture the enlarged image of printed sample. Other than that, the dimensions such as layer height, layer width and gap between line were measured. To perform accurate measurement, the calibration of pixel-to-actual length was needed. First, the calibration sheet was placed on top of the sample. Then, in the software ZY, the scale line of software was adjusted to match the scale on the calibration sheet. This involves aligning the software's measurement scale with the known length on the calibration sheet. After that, the matched scale on the calibration sheet

was input back to the software. By completing these steps, it helps in converting pixel measurements to actual lengths, and allow to accurately measure objects viewed under the optical microscope.

Additionally, the samples were cut in half and observed again with an optical microscope to analyze the cross-section of the printed sample and measure the span length, facilitating the study of mechanical properties such as storage modulus and the calculation of macro porosity.

3.11 Scanning Electron Microscopy (SEM)

The surface morphology of the sintered sample was analysed using a Hitachi S-3400N scanning electron microscope (SEM). For solid sample, it was first grind with a grinding machine, starting with coarse grit and progressing to finer grit. The sample was then polished using 3.0 μm diamond paste followed by 1.0 μm diamond paste to ensure a smooth, flat surface. After polishing, a thin layer of a gold-vanadium mixture was applied to coat the sample. This coating helped to maintain the integrity of the original surface morphology, provided a conductive surface for electron beam interaction, and minimized charging effects, thereby enhancing image resolution during SEM imaging. With these preparations completed, the solid sample was ready for SEM examination, allowing for precise measurements of the grain size and detailed observations of the surface morphology. While for powder and scaffold sample, the grinding and polishing process was skipped.

After that, images of the sample were taken at an accelerating voltage of 15.0 kV, using magnifications that varied from ×50 to ×15k.

3.12 Summary

The synthesis of forsterite involved determining the ratio and amount of MgO and hydrophilic fume SiO_2, calculated using their molecular weights: MgO (40.3 g/mol), SiO_2 (60.1 g/mol), and forsterite (140.7 g/mol). For a desired mass of 100 g of forsterite powder, 43.36 g of SiO2 and 57.29 g of MgO were needed, considering an additional 1.5% SiO2 to account for loss during synthesis. The balanced equation was $SiO_2 + 2MgO \rightarrow Mg2SiO_4$.

Mechanical activation started with assembling a high-shear mixer, checking for concentric assembly, and measuring hydrophilic fume SiO_2 in small amounts to increase accuracy. The SiO_2 was mixed with 500 ml of deionized water at 2000 rpm. MgO was measured and added to the mixture, which was then mixed at 4500 rpm for 2 hours. Ethanol was used to prevent sticking, and the mixture was dried in an oven at 90 ℃ for at least 5 hours. The dried mixture was ground into powder and calcined at 1200 °C for 2 hours, with a 3-hour holding time for crystallization, followed by sieving.

X-ray Diffraction (XRD) analysis checked the crystal structure and purity of the forsterite powder, scanning from 10º to 60º at 2º/minute. The data was analyzed using HighScore Plus and visualized with OriginPro. For ceramic ink formulation, based on research by Ang, Tey, and Yeo (2024), the slurry contained 45 vol% solid content, 300 g/L binder concentration, and 1 vol% defoamer, with diethyl phthalate as a plasticizer and BYK 110 as a dispersant. The ink was mixed using a planetary centrifugal mixer, which required 3D-printed fittings for the containers to prevent acetone damage. The ink preparation involved mixing dispersant, plasticizer, and acetone, followed by forsterite powder and ceramic balls, and finally the binder. The mixture was cooled in a water bath to reduce acetone evaporation.

Other than that, test prints using a 3D printer were controlled by g-code from FullControl GCode Designer, offering precise control over printing parameters. Three models were printed: a square thin wall to examine shape fidelity, a scaffold structure for sagging effect and porosity study, and a solid model for XRD, density, and hardness tests. Printing parameters included a layer height of 0.5 mm for the thin wall and solid, and 0.8 mm for the scaffold, with a layer width of 1.2 mm.

Debinding removed the binder, heating at 2 °C/min to 250 °C with a 2-hour hold. Sintering fused the particles, heating at 5 °C/min to 1500 °C with a 2-hour hold. Rheological properties of the ceramic ink were tested using an Anton Paar Rheometer, performing flow sweep, amplitude sweep, frequency sweep, and 3ITT tests.

Lastly, density was measured using water immersion and Archimedes' method. Vickers hardness was tested with a 10 kgf load for 10 seconds, and

values were converted to GPa. An optical microscope with software ZY measured dimensions and analyzed cross-sections. Scanning Electron Microscopy (SEM) examined surface morphology and grain size after grinding, polishing, and gold-vanadium coating, providing detailed images at various magnifications.

CHAPTER 4

RESULTS AND DISCUSSION

4.1   X-ray Diffraction analysis

Figure 4.1 presents the X-ray diffraction (XRD) results for both forsterite powder and a printed forsterite structure, with the intensity plotted against 2θ. The XRD patterns of both samples indicate the absence of impurities such as enstatite or periclase. The similarities in the diffraction patterns suggest that the preparation of the ceramic ink does not negatively impact the crystalline phase or purity of the forsterite material.

The consistency between the XRD results of the forsterite powder and the printed structure implies that the processing techniques used to create the ceramic ink effectively preserve the integrity of the forsterite's crystalline structure. This result demonstrates the suitability of the ink preparation method for maintaining the characteristics of materials. This was essential for ensuring the performance and reliability of the printed forsterite structures.
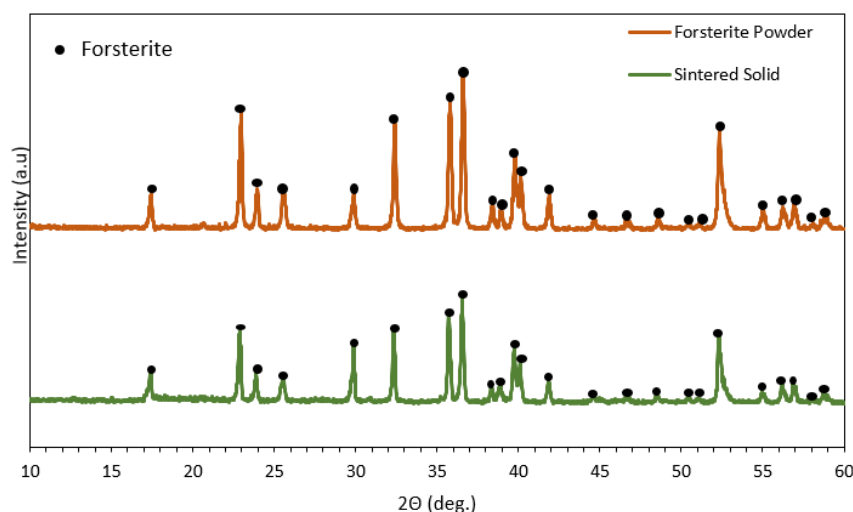
Figure 4.1: XRD pattern of forsterite powder and sintered printed forsterite solid.

4.2   Printability

Figure 4.2 illustrates different formulations of ceramic ink printed onto a thin wall structure with dimensions of $20 \times 20 \times 20$ mm. At a solid loading of 45 vol%, the adhesion between layer-to-layers was weak. Therefore, the thin wall structure lacks sufficient strength of shape fidelity to maintain its integrity. Moreover, the high solid loading results in excessively high viscosity of the ceramic ink, leading to poor extrudability.

After that, the solid loading was reduced to 35 vol% while maintaining a binder concentration of 300 g/L. However, the printed samples were lacked the required strength to retain the desired shape, resulting in the collapse of the thin wall structures. This was due to the structure cannot withstand the weight of the forsterite powder. As additional layers were deposited, the printed structure began to slump. This deformation occurred as the increasing weight of each successive layer added pressure to the structure under it, causing it to lose its shape and stability. The issue remains even when the binder concentration was increased to 400 g/L. In both cases, the reduced solid loading and adjusted binder concentration did not provide sufficient shape fidelity to prevent collapse during the printing process.

The solid loading was subsequently increased to 40 vol% while maintaining a binder concentration of 300 g/L. This adjustment slightly improved the slumping effect, but the weak filament strength led to discontinuous material extrude and resulting in an incomplete printed structure. When the binder concentration was further increased to 400 g/L, the thin wall structure could be printed successfully. However, small agglomerations of ceramic ink were observed on the surface of the printed wall. These imperfections may impact the overall quality and smoothness of the final structure,

Finally, to achieve the optimal formulation, the solid loading was gradually increased to 43 vol% with the goal of improving the smoothness of the ceramic ink during printing. At a binder concentration of 300 g/L, the resulting printed wall surface was smooth. However, the buckling effect appeared due to insufficient shape fidelity strength. Therefore, the binder concentration was increased to 400 g/L. Eventually, a complete thin wall

structure with a smooth surface and excellent shape fidelity was successful printing. This combination of solid loading and binder concentration provided the necessary strength and stability to produce high-quality, structurally sound printed walls.

This observation was also proved in the research conducted by Ang, Tey and Yeo (2024), the insufficient amount of binder concentration led to poor shape fidelity and poor visual quality.
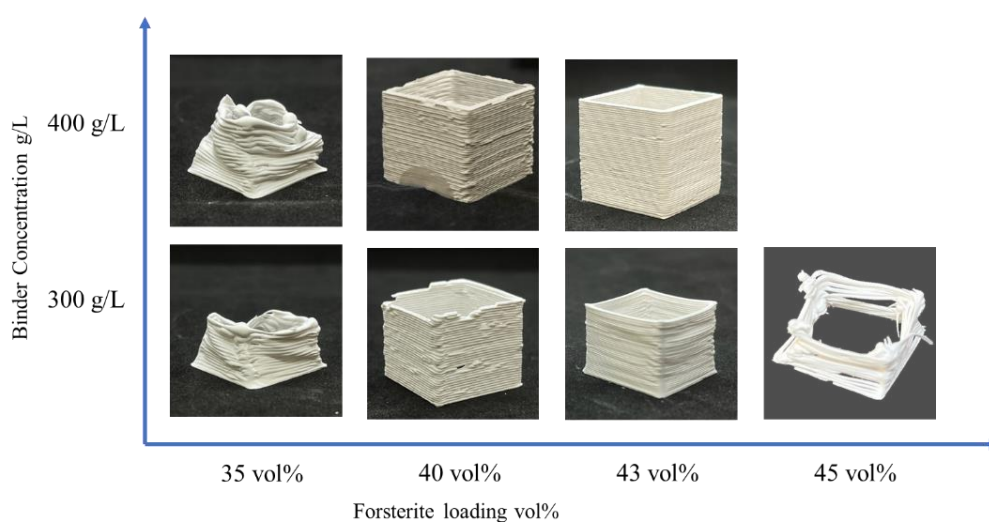

Figure 4.2: Printed thin wall sample with different formulation.

Table 4.1: Table of printability of different ink formulation

Forsterite loading / Binder concentration	35 vol%	40 vol%	43 vol%	45 vol%
300 g/L	Slumping	Poor	Buckling	Unprintable
400 g/L	Slumping	Poor	Good	

4.3 Rheology analysis

From the result obtained in printability test, the formulation of solid loading of 40 vol% with binder concentration of 400 g/L and solid loading of 43 vol% with

same binder concentration were chosen to perform rheology analysis, which include flow curve, amplitude sweep and 3ITT curve test.

4.3.1   Flow curve analysis

In the flow curve analysis, the viscosity of the ceramic ink was measured by increasing the shear rate to determine whether the ceramic ink behaves as a Newtonian or non-Newtonian fluid when undergo extrusion. From Figure 4.3, the viscosity was decreasing while the shear rate increases. Therefore, the ceramic ink could be extruded through the nozzle with minimal force, as its viscosity gradually decreased when subjected to small increases in shear rate. This observation was similar to the result obtained in the research of Aamir and Ismail (2021), both ceramic inks in this project exhibited shear thinning behaviour. The shear rate can be calculated with Equation (4.1) and (4.2).

$$Q = Sr^2 \tag{4.1}$$

$$\dot{\gamma} = \frac{4Q}{\pi r^3} \tag{4.2}$$

Where

Q = Volumetric flow rate (mm^3/s)

S = Printing speed (mm/s)

r = Radius of nozzle (mm)

$\dot{\gamma}$ = Shear rate (s^{-1})

In this project, the printing speed was 6.67 mm/s and the radius of nozzle was 0.6 mm. Therefore, the calculated shear rate was 14.15s^{-1}. From the result obtained, the viscosity of ceramic ink increased from 34.870 Pa.s to 287.26 Pa.s when the solid loading of forsterite increase from 40 vol% to 43 vol%.
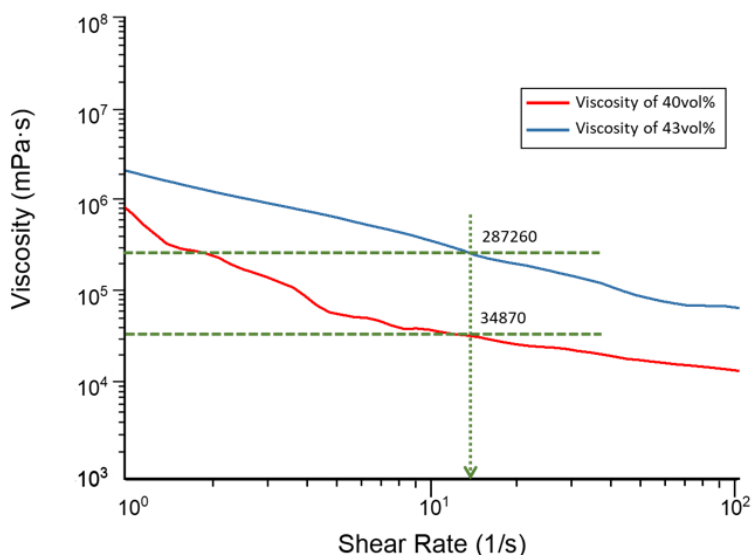
Figure 4.3: Flow curve of ceramic ink of 40 vol% and 43 vol% solid loading.

4.3.2 Amplitude sweep analysis

Figure 4.4 shows the storage modulus and loss modulus, revealing three distinct zones. In the first zone which coloured green, known as the linear viscoelastic region (LVR), the storage modulus (G') remains constant but generally higher than loss modulus (G"). While Point 1 which also known as yield point represents the end of the LVR. If a narrow LVR region was obtained, it indicated that these inks have poor stability and consistency.

The organogel forsterite ceramic ink produced in this project had a significantly narrower LVR region compared to the colloidal ink studied by Laura and Maria (2021). Therefore, it implied that the organogel ink had lower stability and consistency than colloidal ink.

In the second region which was coloured blue. It was the region between points 1 (yield point) and 2 (flow point), the G' remains higher than G", indicating that elastic behaviour predominates over viscous behaviour. The flow point occurs at the intersection point of G" and G', In this region, due to the yield stress was already overcomed, therefore, this region was an irreversible deformation and solid-like behaviour. Lastly, the third region (red) which was after the flow point, the G" exceed G'. It means that the ceramic ink undergoes a transition from a solid-like state to a liquid-like state.

Then, due to the higher storage modulus of 43 vol% ink obtained from Figure 4.4, the graph of storage modulus and loss modulus against shear stress

was plotted to identify the yield shear stress and flow shear stress. From Figure 4.5, the ceramic ink of 43 vol% solid loading has the yield shear stress of 28.05 Pa and flow shear stress of 4183.60 Pa.
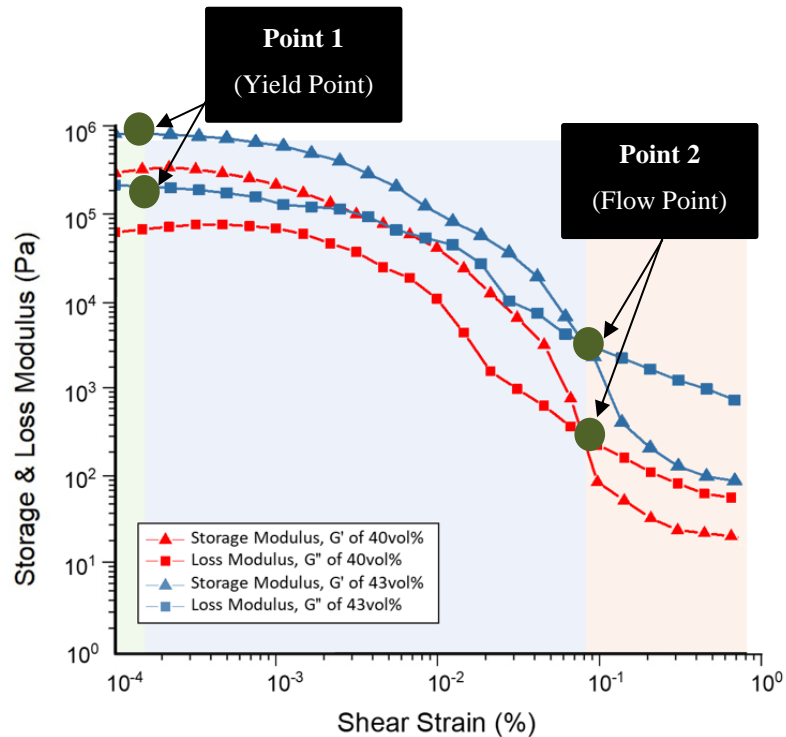

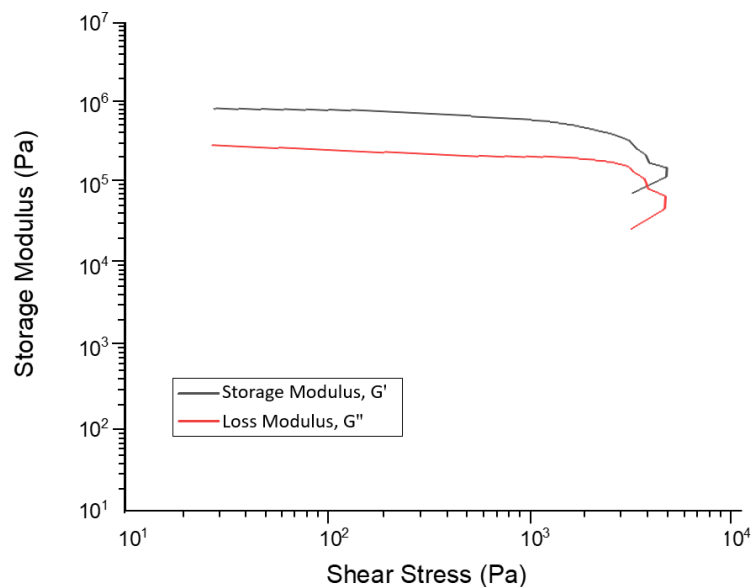Figure 4.4: Amplitude sweep test of ceramic ink of 40 vol% and 43 vol% solid loading.

Figure 4.5: Graph of storage and loss modulus against shear stress of 43 vol% solid loading ceramic ink.

4.3.3   3ITT curve test

There were 3 intervals included in 3ITT curve, which indicates that ink was exhibited a solid-like behaviour of G' higher than G'' in interval 1. After that, the ink was undergoing transition to interval 2 which was liquid-like behaviour. This interval simulates the extrusion process. Lastly, interval 3 exhibits a solid-like behaviour of G' higher than G''.

The main purpose of 3ITT curve test was to study and determine whether the recovery of the solid-like behaviour was fast enough to retain the nozzle shape. Therefore, from Figure 4.6, this ceramic ink has good thixotropic behaviour and good self-supporting capacity after printing. Additionally, in interval 3, the high recovery level implied that this ceramic ink more completely regained its original properties.
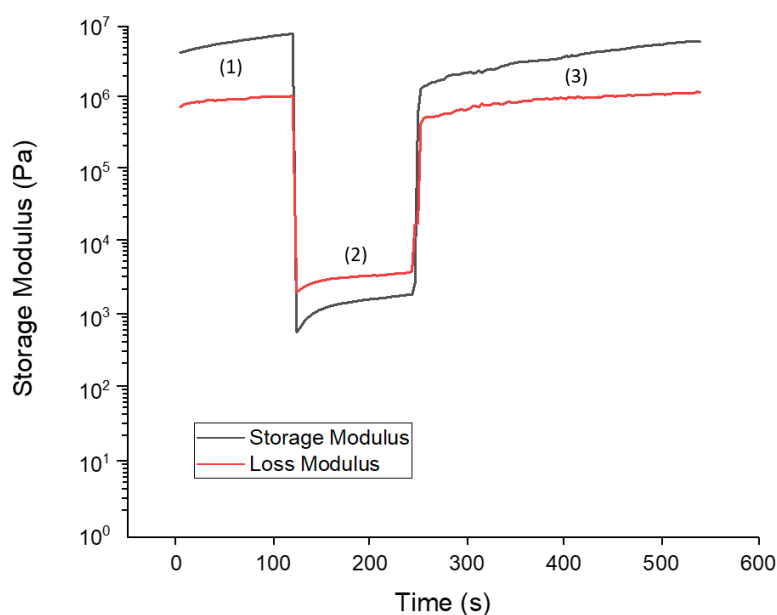
Figure 4.6: 3ITT result of 43 vol% solid loading ceramic ink.

4.4   Physical properties

The sintered ceramic ink with 40 vol% solid loading and 43 vol% solid loading were then performed several tests to study the physical properties of both formulations such as shrinkage, weight loss, density and porosity.

4.4.1 Shrinkage percentage and weight loss

In terms of shrinkage percentage, the dimensions of all printed sample were recorded at 3 stages. These 3 stages were before debinding, after debinding/before sintering and after sintering, where the examples were shown in Appendix C. The shrinkage percentage were calculated and shows in Figure 4.7. Generally, the shrinkage in Z-axis was the highest compared to other two axis. This was due to the gravitational force and weight of the sample itself can compress the sample downward and causing higher shrinkage percentage in Z-axis. The shrinkage was due to the densification process during sintering where the forsterite particles fused together to occupy the space left behind by the solvent.

Other than that, the scaffold structure (lattice) has relatively higher shrinkage percentage compared to other 2 types of models. This was due to the designed macro porosity increase the voids and space within the structure, which lead to higher shrinkage percentage during sintering process. Besides that, scaffold structure also has lesser structural support compared to solid. Therefore, it increases the chance of deformation and shrinkage. Similarly, the thin wall model has higher shrinkage percentage than solid due to the structural support.
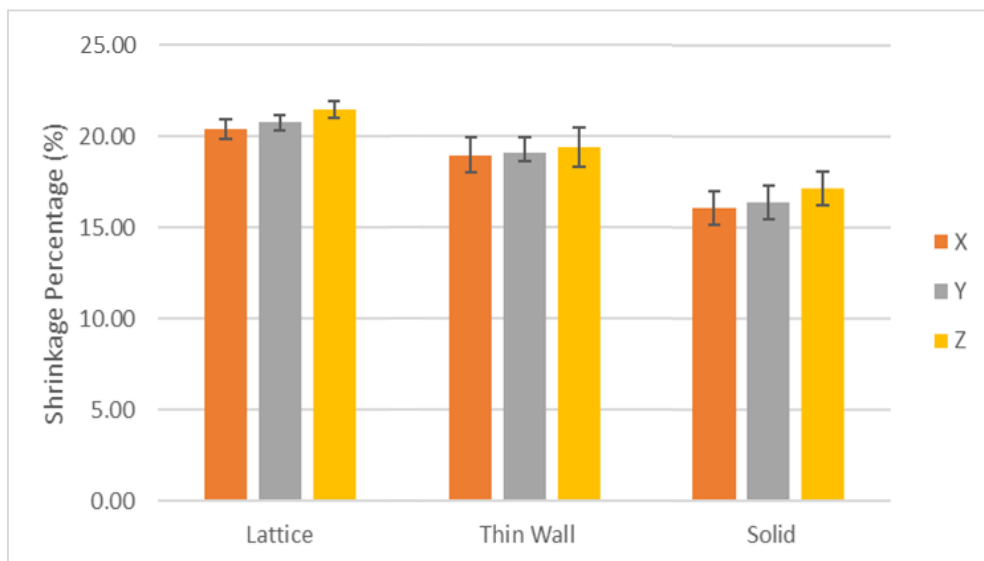
Figure 4.7: Graph of shrinkage percentage of 43 vol% solid loading.

The weight loss caused from green part to final part was due the remove of binder, plasticiser and dispersant. For example, at the solid loading of 43

vol%, when the solvent was evaporated and remain green part, the weight of dried binder was 7.07%, the weight of plasticiser was 9.38% and 6.41% for dispersant. It implies that there were 22.76 weight percentage of additive beside the weight of forsterite. Therefore, from this data, the weight loss after sinter should close to 22.76%. From the measured result, the average weight loss measured for 3 models were recorded as 20.33%, which has 10.67% of difference.
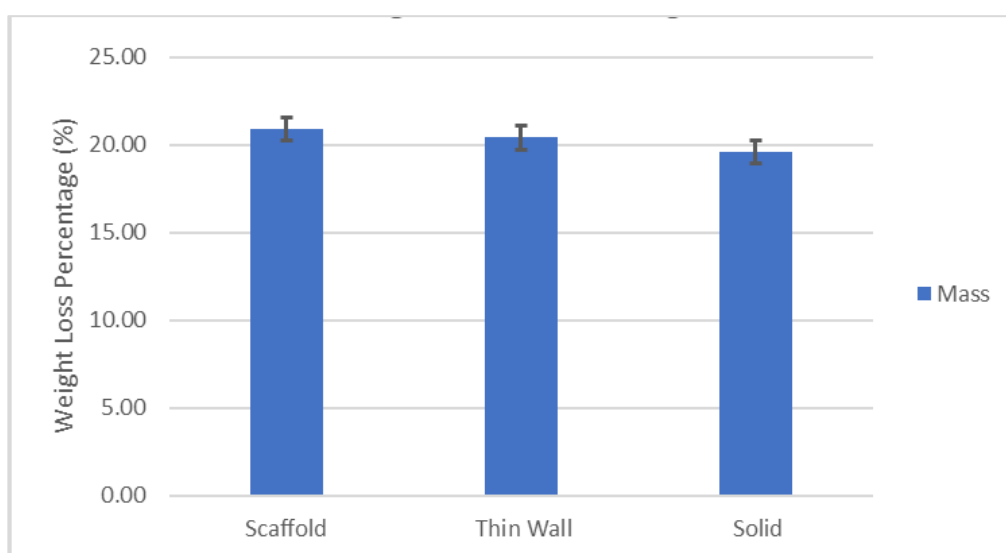

Figure 4.8: Graph of weight loss percentage of 43 vol% solid loading.

After that, the dimension shrinkage percentage and weight loss of both sintered sample from 40 vol% solid loading ceramic ink and 43 vol% solid loading ceramic ink were compared. From Figure 4.9 below, the 40 vol% sample has generally higher percentage in terms of shrinkage and weight loss. This implied that the 40 vol% sample has higher porosity than 43 vol% due to the low solid-to-binder ratio. This was because when the binder percentage was higher in the ceramic ink, indicated more material required to be burned off during debinding and sintering. Therefore, more significant shrinkage and weight loss due to more material being removed. Thus, this result also indicates that ceramic ink with 43 vol% loading has lower shrinkage.
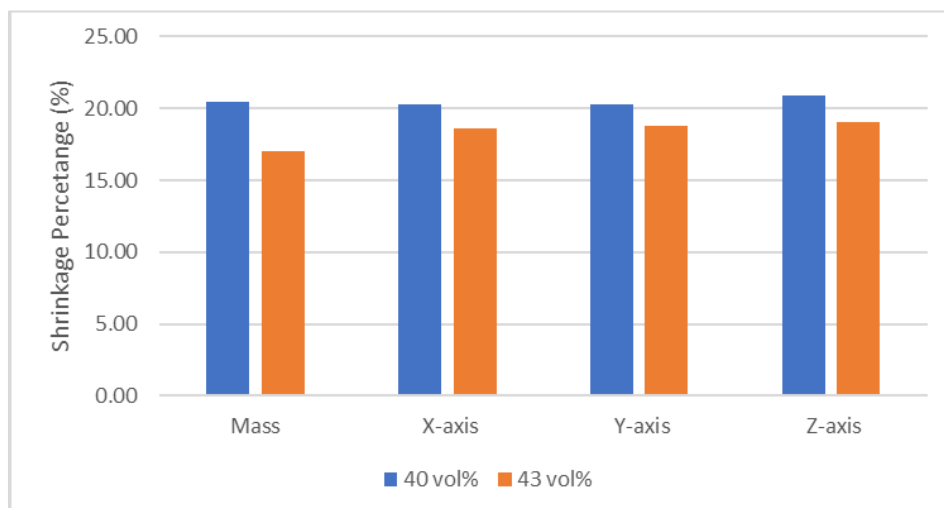
Figure 4.9: Graph of shrinkage and weight loss percentage of printed sample
from solid loading of 40 vol% and 43 vol%

4.4.2   Density test

The density of the sintered sample was determined using the Archimedes method, where the dry weight, weight when immersed in water, and weight in air after immersion in water were recorded for each sample. The square thin wall model and solid model were used to perform density test. Sample for both 40 vol% solid loading ink and 43 vol% solid loading sintered sample were involved in this density test. From Figure 4.10, the bulk density of 40 vol% sintered sample was calculated to be 2.65 ± 0.02 g/cm^3, which was lower than the density of 43 vol% sintered sample at 2.70 ± 0.01 g/cm^3.

While compare the measured density to the theoretical density of forsterite at 3.275 g/cm^3, the density of 43 vol% sintered sample was 82.30% to theoretical density. However, density of 40 vol% sintered sample has only 80.89% to the theoretical density of forsterite. Therefore, this result indicate that 43 vol% solid loading sintered sample has the density which closer to theoretical forsterite density. Additionally, the density was also inversely proportional to the porosity, which mean the higher the porosity, the lower the density. Thus, this result also implies that 40 vol% has more porosity than 43 vol%
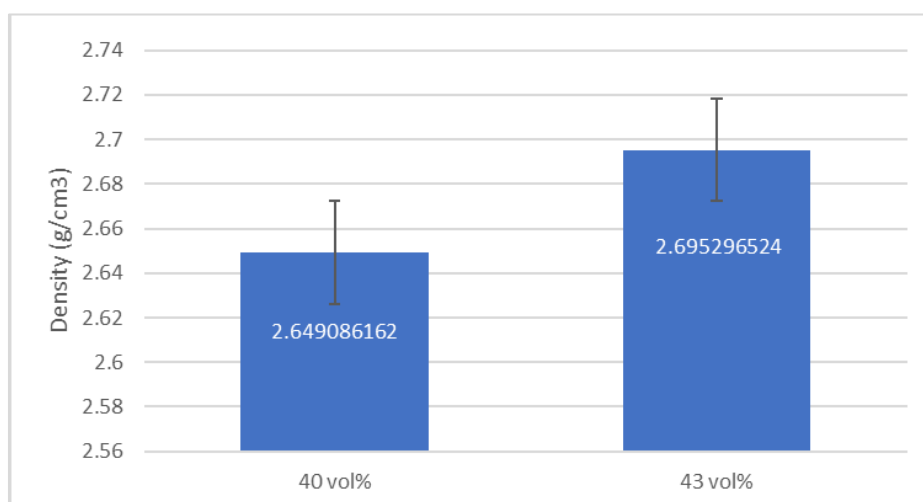
Figure 4.10: Graph of density of printed sample from solid loading of 40 vol%
and 43 vol%.

4.4.3 Porosity

In this project, the macro porosity and micro porosity were considered. The macro porosity was the designed porosity of the structure during printing, which decided by the layer-to-layer height, span length and filament size. However, the micro porosity was the porosity include in the material when print. To ensure the consistency of the porosity of the material, the density, which was the mass over volume of the sample was compared with the macro porosity and micro porosity. To fulfil both macro and micro porosity variable, scaffold structures of 43 vol% solid loading were used as reference. From Appendix C-1, the dimension of scaffold model were 17.12 mm, 17.30 mm and 15.24 mm, and the total volume of 43 vol% scaffold structure was calculated as 4.514 cm^3, and the weight of 9.554 g. Therefore, the density of the sample was 2.116 g/cm^3. By using Equation (3.9), the total porosity was calculated to be 35.37%. Theoretically, the combination of micro porosity and macro porosity should have close to 35.37%.

In terms of macro porosity, the cross section of scaffold structure was measured with optical microscope and software ZY as shown in Figure 4.15 (a), (b) and (c). The measured average layer-to-layer height was 0.55 mm, layer width of 0.89 and span length of 1.38mm. After that, the volume of cylinder intersects, v_i was measured to identify the intersect percentage of cylinder. Because of the intersect was less than 1% of total volume of the structure, the

simplified formula of macro porosity was used as in Equation (2.5). After that, the calculated macro porosity was 18%.
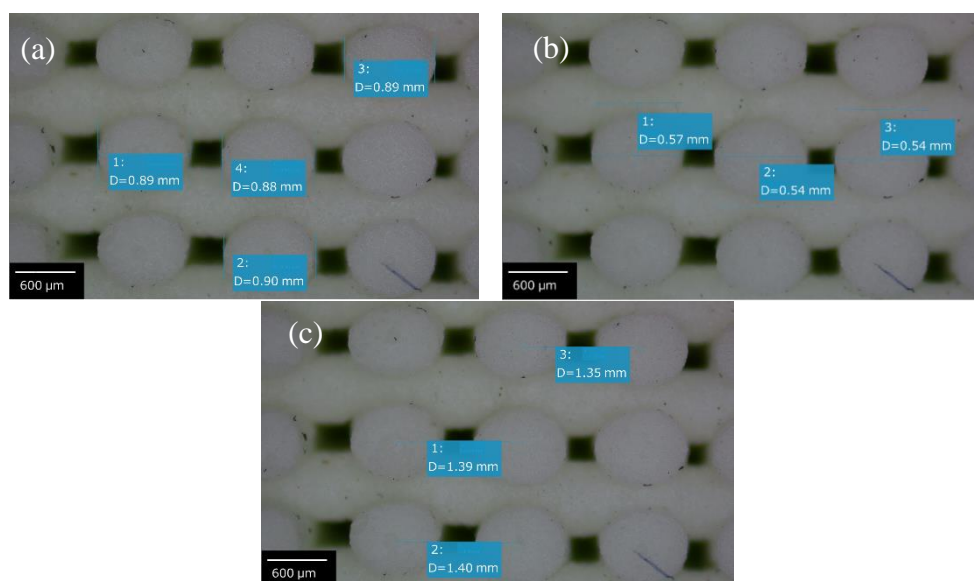

Figure 4.11: Cross section of scaffold structure with measurement of (a) layer width, (b) layer-to-layer height, (c) span length.

Using Equation (2.6), the microporosity was calculated based on the density of the 43 vol% sintered sample, which was 2.71 g/cm³. The calculated micro porosity was recorded as 17.28%. Then, the macro porosity of 18% was added with micro porosity of 17.28% and provide to total porosity of 35.28%. When comparing with the measured porosity of mass and volume from Equation (3.7) and found to be 35.37%, the percentage error was only 0.25%. Therefore, it implies that the parameters measured and used in calculation were reliable. It also demonstrated the reliability of this calculation method.

Then, the micro porosity from both 40 vol% and 43 vol% ceramic inks were further study by determining the apparent porosity and closed porosity. Generally, the apparent porosity was the interconnected pores from the surface, closed porosity was the isolated and sealed pores within the surface. From Figure 4.12, the SEM of cross section of scaffold structure was analysed to study the closed porosity inside the printed filament. From the result obtained, the closed porosity was significantly higher than the apparent porosity. The apparent porosity can be observed in Figure 4.15.
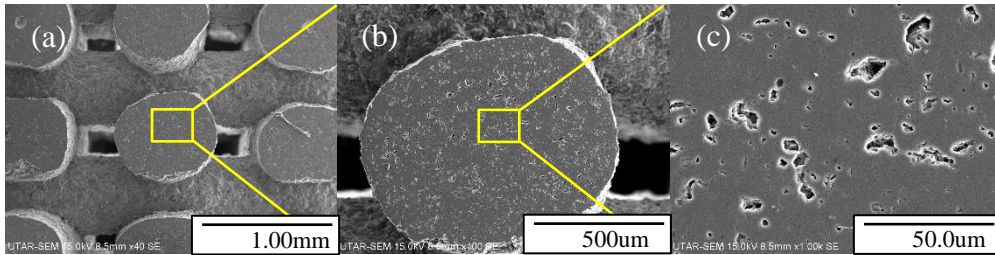
Figure 4.12: SEM of 43 vol% scaffold with magnification of (a) ×40 (b) ×100 (c) ×1k.

Figure 4.13 shows the calculated apparent and closed porosity based on Equation (3.9) to (3.11). Generally, the closed porosity was around 5 to 7 times more than apparent porosity. Therefore, it supports the observation made in last paragraph. Besides that, Figure 4.17 also indicates that ceramic ink of 43 vol% solid loading resulted less porosity than 40 vol%.
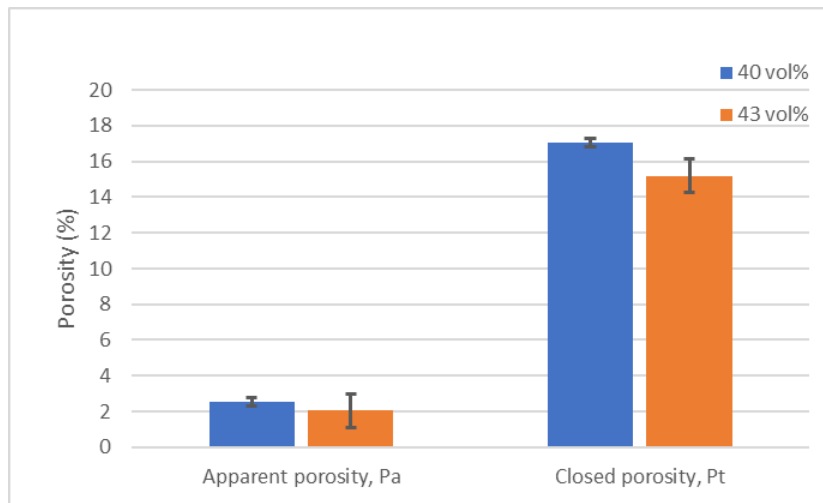

Figure 4.13: Graph of apparent and closed porosity of 40 vol% and 43 vol% solid loading ceramic ink.

4.5 Scanning Electron Microscopy (SEM)

The surface morphology of the green part and the final part with a solid loading of 43 vol% was analyzed using SEM to study the changes before and after the sintering process. Figure 4.14 shows the SEM result with the magnification of ×50, ×3k and ×15k of green part, where the acetone was considered fully evaporated. While Figure 4.15 shows the SEM result of sintered final part after polishing with magnification of ×50, ×3k and ×15k. From Figure 4.14 (c), the

binder can be seen clearly in the green part, which was binding the forsterite particle together. In Figure 4.8, the binder was significantly removed after debinding process and sintering process. Therefore, it implies that the debinding temperature of 250 ºC was sufficient to remove the CDB binder. The microstructure of all the sintered specimens was crystalline solid form.

However, the particles have only reached the necking stage without fully grains forming. This indicates that the sintering temperature was insufficient for full grain formation. Incomplete grain formation during sintering results in voids or pores between particles, reducing the density of the sample. Therefore, the density of 43 vol% sintered sample only reached 82.30% to theoretical density of forsterite.
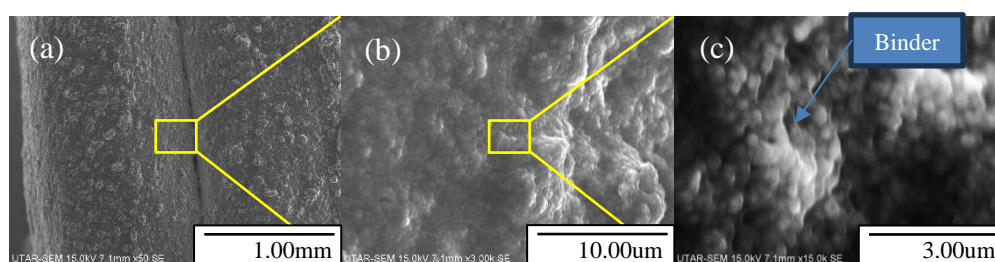
Figure 4.14: SEM of 43 vol% green part before debinding process of magnification with (a) ×50 (b) ×3k (c) ×15k.

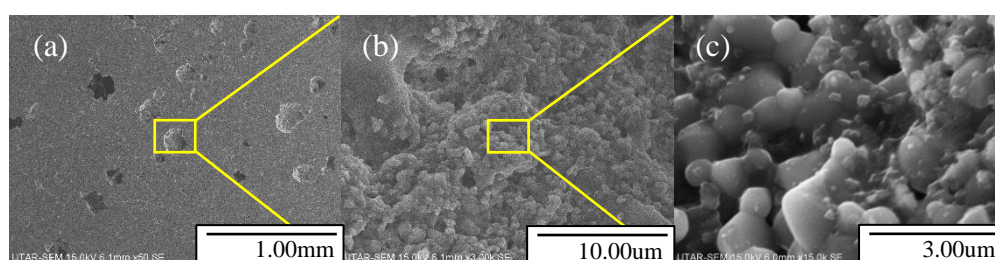Figure 4.15: SEM of 43 vol% final part after polishing with magnification of (a) ×50 (b) ×3k (c) ×15k.

After that, the number of apparent pores and apparent pore size were also compared for both 40 vol% and 43 vol% solid loading. Generally, the 40 vol% has higher pore distribution across the surface compared to 43 vol%. Therefore, it indicates that the formulation of 40 vol% has higher apparent porosity than 43 vol%, this observation was further proved the 40 vol% solid loading sample has lower density and higher porosity than 43 vol% ink.
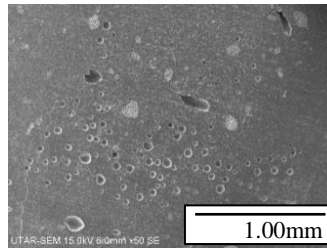
Figure 4.16: SEM of 40 vol% final part with magnification of ×50.

4.6   Vickers Hardness Test

Vickers Hardness Tests were conducted on solid samples sintered and polished at both 40 vol% and 43 vol% solid loading. From the result obtained, the sample of 40 vol% has the average Vickers hardness of 344.17 ± 39.16 HV, while 43 vol% has the average Vickers hardness of 508.63 ± 52.96 HV.

These data were then converted to GPa with the Equation (3.14) and plotted in Figure 4.17. The sample with 40 vol% has the average Vickers hardness of 3.38 ± 0.38 GPa and 4.99 ± 0.52 GPa for 43 vol%. Therefore, it indicates that printed sample from 43 vol% solid loading has greater hardness than 40 vol%. Other than that, by comparing the result with porosity, it also implies that the higher the porosity, the lower the hardness. This was due to the porosity will become a stress concentrator that will deteriorate the mechanical properties of the sample such as hardness. This result was matched with the conclusion made by Pecqueux, et al. (2010), the higher porosity led to poor mechanical properties performance.
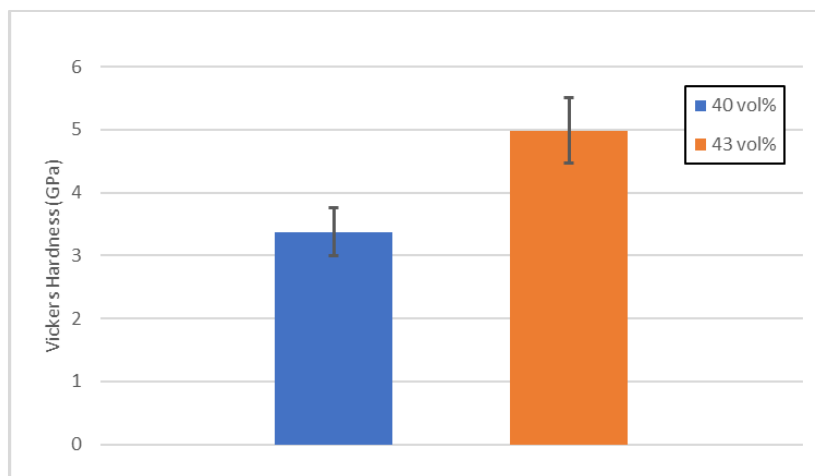

Figure 4.17: Graph of Vickers hardness of 40 vol% and 43 vol% solid loading ceramic ink.

CHAPTER 5

CONCLUSION AND RECOMMENDATIONS

5.1   Conclusion

In summary, the synthesised forsterite powder shows minimum impurity. Therefore, the reliability of the method to synthesise forsterite powder was proven. After that, the XRD for printed and sintered forsterite structure has similar pattern with forsterite powder. It implies that this formulation and method of preparation of ceramic ink preserves the crystalline phase and purity of forsterite. Therefore, the first objective of synthesise forsterite powder using mechanical activation method was achieved.

Then, different combination of binder concentration and solid loading were tested for the printability. 7 formulations were prepared from 35 vol% solid loading to 45 vol% and binder concentration from 300 g/L to 400 g/L. The formulation 40 vol% and 43 vol% with binder concentration of 400 g/L shows the best printability result among 7 ceramic ink formulations. There was minimum slumping effect or discontinues extrusion happened. In terms of rheology, both ceramic inks exhibit shear thinning behaviour as their viscosity decreases with increasing shear rate. At the shear rate of $14.15s^{-1}$, viscosity of 40 vol% ink was 34.870 Pa.s and 43 vol% was 287.26 Pa.s. This indicated the viscosity of ceramic ink was directly proportional to the solid loading. Other than that, 43 vol% ink also showing greater storage modulus and loss modulus than 40 vol% ink. The 43 vol% ink has yield shear stress of 28.05 Pa and flow shear stress of 4183.60 Pa. By comparing with 40 vol% ink, 43 vol% ink was more viscous and higher structural stability when printing. From 3ITT, the 43 vol% ink also behaves as expected, which also implies that this ink has consistent performance and stability. As a result, the objective 2 and objective 3 had been achieved.

Other than that, the SEM analysis reveals that the debinding and sintering processes effectively remove the binder and increase grain size. The 43 vol% ink formulation shows lower apparent porosity and more consistent pore size compared to 40 vol%, indicating better porosity control and suitability

for 3D printing applications. In term of physical properties, the 43 vol% solid loading ceramic ink demonstrated better dimensional stability and weight stability than 40 vol%. The density measured for 43 vol% sintered sample was 2.70 ± 0.01 g/cm^3 which was higher than 40 vol% sintered sample. It also leads to greater hardness due to lower porosity in 43 vol% sintered sample. Thus, the objective 4 was also achieved.

In conclusion, the formulation with 43 vol% forsterite loading, 400 g/L binder concentration, 32 vol% acetone, 15 vol% plasticiser, and 10 vol% dispersant achieves optimal results in terms of printability, rheological behaviour, dimensional stability, weight stability, density, porosity and hardness.

5.2   Recommendations for future work

As mentioned in Subtopic 4.5, the sintering temperature was a crucial factor in determining the density and mechanical properties of the sintered sample. Due to the constraint of furnace temperature, the sintering temperature was set to be 1500 $^\circ$C. Further investigation into alternative heating temperatures and varying holding times could be conducted to identify the optimal conditions for achieving the best results in the sintering process.

Other than that, only 7 different combinations of ceramic ink formulations were tested to optimize the formulation in this project. Therefore, further investigation into a broader range of forsterite ceramic ink formulations could help determine the maximum density, hardness or enhance other physical and mechanical properties.

In addition to density and hardness tests, other physical and mechanical properties can be evaluated to study the characteristics of different ceramic ink formulations. For example, tensile strength tests measure the material's resistance to being pulled apart, while compressive strength tests assess its ability to withstand compressive forces.

Lastly, the printing quality can be enhanced by performing linear advance analysis to forecast the pressure build-up in the extruder at high-speed printing conditions. More complex geometry such as gyroid structure can be test to study printability of ink and finishing of the printed part after sintering.

REFERENCES

Aamir, S. and Ismail, L., 2021. Direct ink writing (DIW) of structural and functional ceramics: Recent achievements and future challenges. Composites Part B: Engineering, Volume 225.

Achim, S., Tony, S., Silke, E. S., Leonhardt and Bernd, O., 2011. Ball milling in organic synthesis: solutions and challenges. Chemical Society Reviews, Volume 40, pp. 2317-2329.

Belgin, P., A. S., Lenka, C. and M. E., 2023. Rheological Behavior and Printability Study of Tri-Calcium Phosphate Ceramic Inks for Direct Ink Writing Method. Polymers, Issue 15(6), p. 1433.

Budi, A. and Jie, Z., 2014. Fabrication of Metallic Biomedical Scaffolds with the Space Holder Method: A Review. Materials, Volume 7(5), pp. 3588-3622.

Catarina, F. M., Fidel, H. P., Ana, M., Sonia, F., Sandra, I. V., Susana, O., Pedro, M. and Jose, M. F., 2016. Biphasic calcium phosphate scaffolds fabricated by direct write assembly: Mechanical, anti-microbial and osteoblastic properties. Journal of the European Ceramic Society.

Claudio, L., D. C and Brian, S. M., 2002. The use of polymeric milling media in the reduction of contamination during mechanical attrition. Journal of Materials, Volume 17(12), pp. 2997-2999.

Coleman, S. C. and Beeré, W. B., 1975. The sintering of open and closed porosity in UO2. The Philosophical Magazine: A Journal of Theoretical Experimental and Applied Physics, 31(6), pp. 1403-1413.

Espinal, L., 2012. POROSITY AND ITS MEASUREMENT, Gaithersburg: National Institute of Standards and Technology, Gaithersburg, MD, USA.

Francisco, C. N., Mauricio, V. G., Guilherme, O. N., Claudio, A., Marcelo, T. S., Cristiano, B. and Aoisio, N. K., 2022. An Overview of Highly Porous Titanium Processed via Metal Injection Molding in Combination with the Space Holder Method. Metals, Volume 12(5), pp. 783.

FullControl., 2024. FullControl GCode Designer. [Online] Available at: https://fullcontrolgcode.com/ [Accessed 1 April 2024].

Hadi, S., Erfan, O., H. H, Jin, J., Lester, C.G., Rommel, G.B. and Jenneke, K., 2021. Cellulose and its derivatives: towards biomedical applications. Cellulose, Volume 28, pp. 1893-1931.

He, L., Liu, Y., Liu, Y., Hu, K., Lu, K. and Ling, J., 2020. Effects of Solvent Debinding on the Microstructure and Properties of 3D-Printed Alumina Ceramics. ACS Omega, pp. 27455–27462.

Hinton, T. J., Jallerat, Q., Palchesko, R. N., Park, J. H., Grodzicki, M. S., Shue, H. J., Ramadan, M. H., and Hudson, A. R., 2015. Three-dimensional printing of complex biological structures by freeform reversible embedding of suspended hydrogels. Science Advances, Volume 1(9).

Hochstein, B., n.d. Rotational Rheometry. [Online] Available at: https://www.mvm.kit.edu/english/697_786.php [Accessed 2 April 2024].

Huang, R, Joseph, E. R., Myoeum K, Jo. K. H., Lee. S. K., Greogory, N. M. and Choi, J. W., 2021. Material extrusion and sintering of binder-coated zirconia: Comprehensive characterizations. Additive Manufacturing, Volume 45, pp. 102073.

Iishi, K., 1978. Lattice dynamics of forsterite. Ameilcan Mineralogis, Volume 63, pp. 1198–1208.

Jakus, A.E., Geisendorfer, N. R. and Lewis, P. L., 2018. 3D-printing porosity: A new approach to creating elevated porosity materials and structures. Acta Biomaterialia, Volume 72, pp. 94-109.

Jennifer A, L., 2006. Direct Ink Writing of 3D Functional Materials. Advanced Functional Materials, Volume 16(17), pp. 2193–2204.

Jinge, L. and Peng, W., 2022. Metal vaporization and its influence during laser powder bed fusion process. Materials & Design, Issue 215.

Jisu, Das., Bedanta, B., Jagya, J. D. and Tirna, P., 2021. ORGANOGEL: AN IDEAL DRUG DELIVERY CARRIER. World Journal of Pharmaceutical Research, 10(8), pp. 446-465.

Kai, Z., Dauyuan, Y., Zhenfei, Y., Yachao, M., Sheng, Z., Ruichao, L., Jie, L., Junyan, C. and Huiyu, Y., 2020. Additive manufacturing of SiO2–Al2O3 refractory products via Direct Ink Writing. Ceramics International, Issue 46, pp. 27254-27261.

Kassoum, B., Gisèle, L., Mohamed, S., Michael, F., Philippe, B. and Claire, P., 2022. Comparative Properties of Porous Phyllosilicate-Based Ceramics Shaped by Freeze-Tape Casting. MDPI, pp. 75-95.

Kharissova, O. V., Kharisov, B. I., C. M. O. G., Mendez, Y. P and Lopez, I., 2019. Greener synthesis of chemical compounds and materials. MDPI, pp. 191378.

Kosanović, C., Stubicar, N., Tomasic, N., Bermanec, V. and Stubicar, M., 2005. Synthesis of a forsterite powder by combined ball milling and thermal treatment. Journal of Alloys and Compounds, 389(1-2), pp. 306-309.

Laura, M. B. and Maria-Pau, G., 2021. Rheological characterisation of ceramic inks for 3D direct ink writing: A review. Journal of the European Ceramic Society, pp. 18-33.

Leïla, K., Pascal, H., Guillaume, O. and Y. M. G., 2021. Effect of the solvent on the mechanical and structural properties of N-alkyldiamide organogels, Bordeaux: University of Bordeaux.

Mercurio, D. S., 2020. Comparing Lancaster Products K1 Series High Shear Mixer with Conventional Ball Milling. A Simple Mixing Study for Perovskite Ceramics.

Monica, T., Andrea, F., Francesca, R. and Massimo, B., 2021. 3D printable magnesium-based cements towards the preparation of bioceramics. Journal of Colloid and Interface Science, pp.24-35.

Nisar, U. K., Juyeon, L., Sangwoo, K., Daekyung, S. and Hyungjun, K., 2023. Pluronic F-68 and F-127 Based Nanomedicines for Advancing Combination Cancer Therapy. Pharmaceutics, Issue 15(8), pp. 2102.

Ouriel, W., 2023. Hyaluronic Acid absorbs a maximum of 30 times its weight in water. [Online] Available at: https://www.oumere.com/blogs/news/hyaluronic-acid-absorbs-a-maximum-of-30-times-its-weight-in-water [Accessed 3 April 2024].

Pascal, B., Mani, D., David, J. M. and Sander, C. G. L, 2022. Self-Healing Injectable Hydrogels for Tissue Regeneration. Chemical Reviews, Issue 123, pp. 834-873.

Pattaraporn, P., Suruk, U., Pornchai, R., Chuda, C., Warintorn, R. and Pensak, J., 2020. Hydroxypropyl Methylcellulose E15: A Hydrophilic Polymer for Fabrication of Orodispersible Film Using Syringe Extrusion 3D Printer. Polymers, Issue 12(11), pp. 2666.

Pecqueux, F., Tancret, F., Payraudeau, N. and Bouler, J. M., 2010. Influence of microporosity and macroporosity on the mechanical properties of biphasic calcium phosphate bioceramics: Modelling and experiment. Journal of the European Ceramic Society, Issue 30, pp. 819-829.

PrintWiki, 2023. PrintWiki. [Online] Available at: https://printwiki.org/Solvent [Accessed 13 April 24].

Ratnawulan, R. and Ahmand, F., 2020. Recent Advances in Pyrolysis. [Online] Available at: https://www.intechopen.com/chapters/69964 [Accessed 5 September 2023].

Robert, F. S., Filip, I., Wonjae, C., Stephen, A., Morin, Adam A. Stokes, Aaron D. Mazzeo, Xin Chen, Michael Wang, and George M. Whitesides, 2011. Multigait soft robot. Proceedings of the National Academy of Sciences, Volume 108(51), p. 20400–20403.

Rossella, A., and Alberto, F., 2022. FDM Printability of PLA Based-Materials: The Key Role of the Rheological Behavior. Polymers, p. 1754.

Runxiao, Z., Tanvier, S. Q. and Daman, K. P., 2022. 28 - Management of industrial waste and cost analysis. Handbook of Sustainable Concrete and Industrial Waste Management, pp. 595-614.

Shakib, H. S., Paul, J. H., Hongxu, W., Juan, P. E. and Ali, A. H. A., 2022. Lessons from nature: 3D printed bio-inspired porous structures for impact energy absorption – A review. Additive Manufacturing, Volume 58, pp. 103051.

Sharif, U., Hiroki, K., Akihiko, K. and Doriana, M. D., 2020. A system for designing and 3D printing of porous structures. CIRP Annals - Manufacturing Technology, pp. 113-116.

Simon, S., Agus, R., Wasinton, S. and Rudy, S., 2017. Effect of MgO-SiO2 Ratio on the Forsterite (Mg2SiO4) Precursors Characteristics Derived from Amorphous Rice Husk Silica. ORIENTAL JOURNAL OF CHEMISTRY, Volume 33(4), pp. 1828-1836.

Smallwood, I., 2004. Handbook of Organic Solvent Properties. 1st ed. Tunbridge Wells: Gray Publishing.

Tagliaferri, S., Panagiotopoulos. A. and Mattevi, C., 2020. Direct ink writing of energy materials. Materials Advances, Issue 2, pp. 540-563.

Tavangarian, F. and Emadi, R., 2009. Mechanical activation assisted synthesis of pure nanocrystalline. Journal of Alloys and Compounds, Volume 485, pp. 648–652.

Tavangarian, F. and Emadi, R., 2010. Synthesis of nanocrystalline forsterite (Mg2SiO4) powder by combined mechanical activation and thermal treatment. Materials Research Bulletin, Volume 45, pp. 388-391.

Upik, N., Darminto, D., Triwikantoro, Mochamad, Z. and Suminar, P., 2018. Synthesis and characterization of silica sand-derived nano-forsterite ceramics. Ceramics International, Volume 44, pp. 5543-5549.

Xiang, A., Jing Yuan, T. and Wei Hong, Y., 2024. 3D printing of low carbon steel using novel slurry feedstock formulation via material extrusion method. Applied Materials Today, Volume 38.

Yiliang, C., Xiaolei, S., Xuepeng, J., Xiaohui, W. and Hantang, Q., 2020. Printability of a Cellulose Derivative for Extrusion-Based 3D Printing: The Application on a Biodegradable Support Material. Sec. Polymeric and Composite Materials, Volume 7.

APPENDICIES

Appendix A: Grantt Chart of Project

Appendix A.1:   Gantt Chart (FYP1)

No.	Project Activities	W1	W2	W3	W4	W5	W6	W7	W8	W9	W10	W11	W12	W13	W14
M1	Problem formulation & Project planning	■	■												
M2	Literature review		■	■	■	■	■								
M3	Data gathering					■	■	■	■						
M4	Preliminary testing/investigation									■	■	■	■	■	
M5	Report writing & presentation												■	■	■

Appendix A.2:   Gantt Chart (FYP2)

No.	Project Activities	W1	W2	W3	W4	W5	W6	W7	W8	W9	W10	W11	W12	W13	W14
M1	Preparation of ceramic ink	■	■												
M2	Printability study		■	■	■	■	■								
M3	Rheology analysis					■	■	■	■	■	■	■			
M4	Density test & Hardness test								■	■	■	■			
M5	Poster generation									■	■	■			
M6	Report writing & presentation												■	■	■

Appendix B: FullControl GCode of 2 models

Figure B-1:   FullControl GCode of scaffold model.

Figure B-2:   FullControl GCode of thin wall model.

Appendix C: Information of Printed Model

Table C-1:   Dimension and weight of sample.

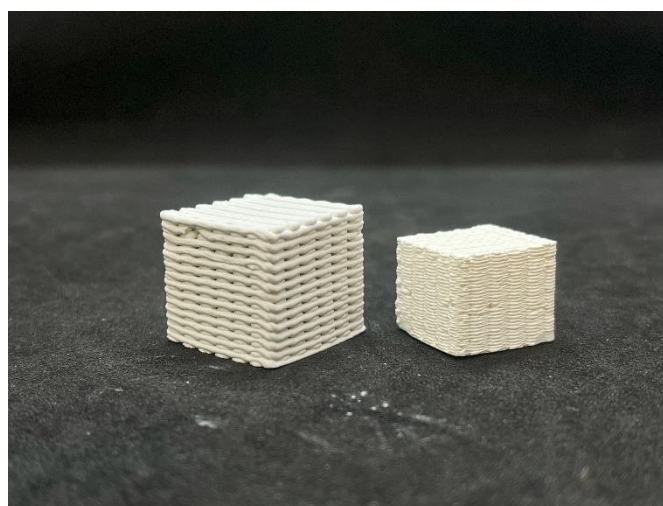| Lattice Structure B (Solid Loading 43vol%)						Before debind	After debind	After sintering
	Mass, g	Mass, g	Mass, g	Shrinkage %				
Sample	12.089	9.991	9.554	20.97				
	Dimension, mm	Dimension, mm	Dimension, mm					
X axis	21.38	21.32	17.12	19.93				
Y axis	21.70	21.70	17.30	20.28				
Z axis	19.42	19.38	15.24	21.52				

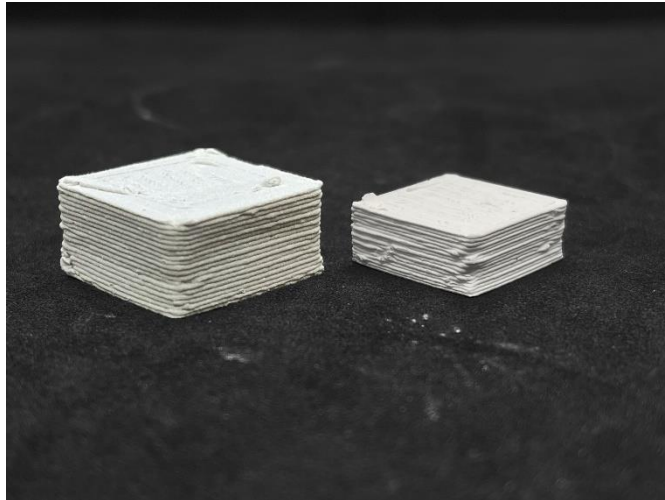Figure C-2:   Scaffold structure before and after sinter process.

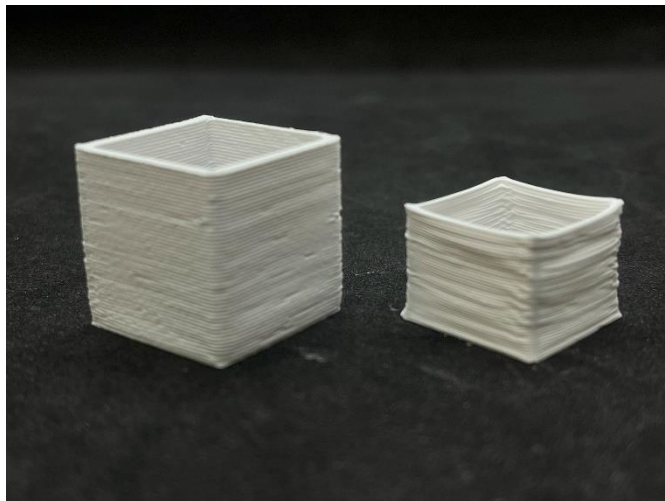Figure C-3:   Solid structure before and after sinter process.

Figure C-4:   Thin wall structure before and after sinter process.